university of groningen

faculty of mathematics and natural sciences

Magneto-elastic transient grating spectroscopy of normal metal/ferromagnetic metal multilayers.

THESIS

submitted in partial fulfillment of the requirements for the degree of

MASTER OF SCIENCE

in

APPLIED PHYSICS

Author :	Darin N. Zwaan
Student ID :	s1993739
Supervisor :	R.I. Tobey
2^{nd} corrector :	P. van Rijn

Groningen, The Netherlands, May 15, 2017

Magneto-elastic transient grating spectroscopy of normal metal/ferromagnetic metal multilayers.

Darin N. Zwaan

Zernike Institute for Advanced Materials, University of Groningen
P.O. Box 221, NL-9700 AE, Groningen, The Netherlands

May 15, 2017

Abstract

Spintronics has become an increasingly popular and important topic, not only in science but in technical applications as well. The use of the spin degrees of freedom offers up exciting discoveries and designs. In this experiment, a non-contact transient grating (TG) spectroscopy method is used to inspect spin dynamics in metallic multilayers that result from ferromagnetic resonance (FMR). Due to the direct generation of sound waves in the sample, magneto-elastic effects excite spin precession in the ferromagnetic layer and possibly external relaxation in the other layers. Using a detection scheme based on Faraday rotation of a probe beam, the magnetization component normal to the sample surface is measured directly and in real time with a temporal resolution in the order of picoseconds. The data is examined in the framework of spin currents and intrinsic and extrinsic relaxation mechanisms, but proved inconclusive on the part of magnetization. Therefore, a future experiment is proposed that should solve the issues found with this experiment.

Acknowledgements

While this work was written by a single author, its creation would have been unthinkable in the absence of several important people. Thanks go to Raanan Tobey for his supervision, teaching and discussions during the project. Additionally, Ronnie Tamming is thanked for his support, company and discussion during many hours of experiments and writing. Although not explicitly involved in the subject of this report, P. van Rijn is also thanked for his supervision and help during the first part of the research. Finally, Chia-Lin receives thanks for his help with setting up the laser and the use of (parts of) his figures to illustrate the experimental set-up.

Contents

Chapter 1

Introduction

Of all the the things that make up modern life, it could be argued that it is the electron that dictates it the most. Without it, very few of modern everyday comforts would exist. Our power, our electronics, even our ability to communicate over long distances (without the use of smoke) comes from this particle. As a consequence, it is not just fundamental science that invests time and research into the electron, but corporations as well. The computer industry for instance, has for a long time aimed to keep up with Moore's Law, a self-fulfilling prophecy that dictates that the amount of transistors on a processor chip will double every 2 years [1]. However, this law is vastly nearing a saturation point, where downscaling induces quantum effects that cannot be ignored or circumvented, not to mention the fact that the materials that make up the transistors have finite length. To relax the first restriction, scientists have directed their attention to spintronics, a field that aims to use the spin angular momentum of the electron to create new and innovative devices. Over the years, spintronics has gained an astonishing amount of attention [2, 3, 4]. Still, new and exciting discoveries are made, for instance on spin transfer torque and spin wave pumping [5].

In this thesis, research is presented on relaxation mechanisms of spins in a ferromagnetic/normal metal bilayer, that could be of importance for various spintronic applications, such as computer memory. First, some theory will be presented that is crucial to understand the experiment and its result. Subsequently the experimental set-up and sample preparation are treated before going into the results and discussion.

Chapter 2

Theory

2.1 Magnetization dynamics

2.1.1 Introduction

Magnets have sparked the interest of scientists for centuries. Devices as old as a thousand years have been discovered in China that utilized a lodestone (a magnet found in nature that received its magnetization from a lightning strike) in order to form a compass [6]. Nowadays, of course, magnets and their inner workings are far less mysterious due to the knowledge the scientific community gained over the ages. After the rise of quantum mechanics in the previous century, leaps have been made towards a fundamental and complete understanding. Nevertheless, magnets and their dynamics are still studied, mostly because in the last decades spintronics has become such a thriving field. The link between the two is, of course, the angular momentum of the electrons. In this section, some elemental discussion is presented on magnetization theory and magnetization dynamics that is necessary to understand and analyze the experimental results. A more detailed derivation of some key concepts is given in the appendix, as their mathematical nature is not necessary to intrepet the results of the experiment presented here.

The magnetic moment μ of an electron is directly related to the angular momentum (L) via its gyro-magnetic ratio γ [7]:

$$\mu = \gamma L \tag{2.1}$$

Evidence of this is found in the Einstein-de Haas effect, where a change in total angular momentum of the electrons is compensated by a opposite change of the material, causing it to rotate. More information on this can be found in reference [7]. Equation

2.1 describes the link between magnetization that stems from the orbital motion of the electron about the nucleus. However, the electron also possesses an intrinsic angular momentum, generally called spin, that can either be $\frac{1}{2}$ or -$\frac{1}{2}$ (in units of $\hbar$). The Hamiltonian of such a spin subjected (only) to an external magnetic field is written as [8]:

$$H = -\frac{g\mu_B}{\hbar} S \cdot B \tag{2.2}$$

Simplifying this to a spin that is either parallel or anti-parallel, this brings along an energy equal to:

$$E = -g\mu_B m_s B \tag{2.3}$$

The equation above describes an energy shift that causes splitting of the levels of the electron that is called Zeeman splitting. The minus sign signifies that the energy is minimized when the spin is parallel to the applied magnetization. In the band structure of metals, it can be visualized as a shifting of the bands with respect to their 0 field positions as shown in Figure 2.1. This is called Pauli paramagnetism and causes the spins to align to an externally applied magnetic field. This strong effect of magnetic fields on spins allows for some interesting manipulations, some of which will be exploited in this experiment.

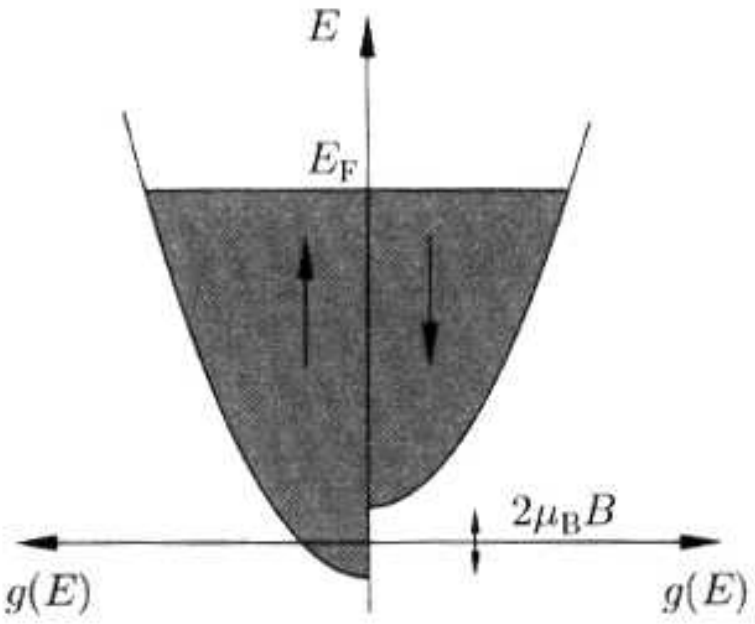

Figure 2.1: *Density of states shifted between spin up and down due to a magnetic field. Adapted from [7].*

2.1.2 Ferromagnetism

In contrast to the alignment of spins in an externally applied magnetic field, cases exist where the spins align spontaneously, actually causing an internal magnetic field. Whether this happens or not depends on the material in question, the temperature and in particular the exchange interactions [7]. Materials that show this behaviour are called ferromagnetic. If the exchange constant, J, is positive this spontaneous alignment is favourable [9]. For more information on exchange interactions see Appendix A.1

Mean field theory attempts to explain ferromagnetism through an exchange field, arising from exchange interactions, which drives spins to align, while temperature seeks to distort this ordering of magnetic moments. This field is created by the alignment of the spins themselves and therefore might feel like something of a circular reasoning, but it suffices to look at the energies to examine whether the system will seek out this configuration. Should it be energetically favorable, the spins in the material will align.

2.1.3 Magnons

The discussion so far has focused on the equilibrium behaviour of spins. However, as it is in all of physics, finite temperature and extrinsic influences cause excitations. In 1930, Bloch posed a theory on the excitations in spin, that is nowadays called a spin wave or magnon [10, 11]. Figure 2.2 shows a representative picture of the magnon. Considering an equilibrium of all spins aligned in the same direction, Bloch realized

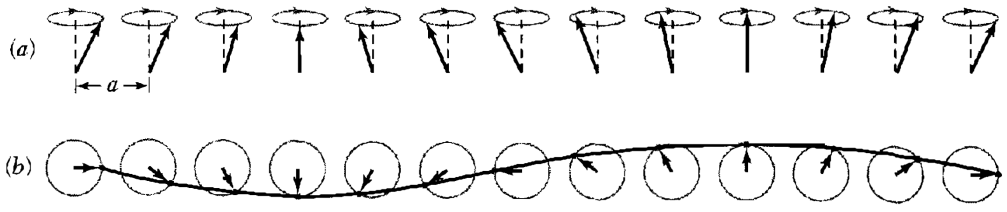

Figure 2.2: *Magnon, a quantized spin wave, consisting of one unit of reversed spin spread out over multiple spins, shown in perspective (a) and from above (b). The solid line marks one wavelength. Adapted from [9]*

that instead of flipping one spin in itself, a joined reorientation of several adjacent spins is a lower energy excitation [9]. Following the exchange that is described by the 1D Heisenberg model (equation A.6) and applying it to this system of N spins, assuming only nearest neighbour interactions, one arrives at the following equilibrium exchange

energy:

$$U_0 = -2NJS^2 \tag{2.4}$$

When one of the spins is flipped, it interacts with 2 others, in the opposite way it did before. Therefore, $4JS^2$ energy gain is missed, as well as an additional energy cost of the same magnitude is created, summing to a total energy difference with equilibrium of $8JS^2$. This energy is higher than that which can be derived for the magnon. For instance, in a cubic lattice with lattice constant a it is given by:

$$\hbar\omega = 4JS(1 - cos(ka)) \tag{2.5}$$

(for a detailed derivation, see [9]). It is for this reason that a system of spins is not excited by flipping a single spin, but rather a spin wave (magnon) is created, where the excitation is shared over multiple spins.

Magnons are very similar to other bosons like photons and phonons and are quantized in the same way, with each excitation mode separated by 1 unit of $\hbar\omega$:

$$\epsilon_k = \hbar\omega(\frac{1}{2} + n_k) \tag{2.6}$$

They can also be excited in the same way, provided the energy gap is exactly bridged. Due to the similarity of magnons and phonons, it opens up exciting possibilities for 1 to 1 excitations, due to phonon-magnon interactions. An example of such a process is treated in the section on FMR.

2.1.4 Precession

The precession seen in magnons is not the only one found when looking at the magnetization dynamics of electrons. Consider a magnetic moment μ that lies in a magnetic field, B, with an angle of θ with respect to B [7]. The magnetic field exerts a torque on the magnetic moment equal to:

$$G = \mu \times B \tag{2.7}$$

Since the magnetic moment is directly correlated to angular momentum, as discussed at the start of this chapter, this can be rewritten to:

$$\frac{d\mu}{dt} = \gamma\mu \times B, \tag{2.8}$$

where γ is the gyromagnetic ratio. A simple solution can be reached when one considers a field that lies only in the z direction [6]. Solving the differential equations, one

finds that μ_z is independent of time and both the x and y components oscillate:

$$\mu_x(t) = |\mu| sin(\theta) cos(\omega_L T) \tag{2.9}$$

$$\mu_y(t) = |\mu| cos(\theta) sin(\omega_L T) \tag{2.10}$$

$$\mu_z = |\mu| cos(\theta) \tag{2.11}$$

Here $\omega_L = \gamma B$ is called the Larmor precession frequency, the frequency with which the magnetic moment precesses around the applied magnetic field. The collection of equations can be swept together in the following equation:

$$\frac{dM}{dt} = -\gamma \mu_0 M \times H_{eff} \tag{2.12}$$

The same result holds for a collective of spins. This is proven in A.2, using the quantum mechanical derivation. Equation 2.12 is known as the Landau-Lifshitz equation of motion [12]. It describes a precessional motion that in this idealized case could go on indefinitely. However, as in every field in physics, no such thing exists. This is especially true for the magnetic precession, which is far shorter than that of the nuclei (for instance used in an MRI) [7]. The reason for this is the strong coupling of the electrons to the lattice vibrations. However, this magneto-elastic coupling can also be used to the advantage of these precessions, as described in section 2.1.6.

2.1.5 Damping

The magnetic moment prefers to lie along the externally applied field and will eventually spiral to it [6]. To incorporate this into the equation of motion, Gilbert added a damping term in 1955, resulting in the now widely known (and used) Landau-Lifshitz-Gilbert (LLG) equation [13, 14, 15]:

$$\frac{dM}{dt} = -\gamma M \times H_{eff} + \alpha M \times \frac{dM}{dt} \tag{2.13}$$

Another method of introducing damping was proposed by Landau and Lifshitz themselves, but it is nowadays rarely seen. The effect of the Gilbert damping constant (α) is shown in Figure 2.3. The magnetic moment is shown in Figure 2.3 (a) in its starting position, with the path to equilibrium depicted as a solid line.

The introduction of the Gilbert damping term was done independent of the attempts to understand its origin. Even now, decades after it was introduced, it is still subject to some speculation [16]. Nevertheless, it is commonly assumed that the re-

laxation mechanisms responsible for the Gilbert damping are results of the Spin-Orbit coupling [17]. Models to understand this have been developed, but are far beyond the scope of this thesis. Reference [17] lays out some of them. Simply put, spin orbit coupling opens up the way for several relaxation mechanisms for the spins, like magnon-phonon (1-1,1-2 and 2-1) and magnon-magnon (2-4) [18].

The Gilbert damping constant is considered to be a material property, explaining only intrinsic damping. Incorporating environmental contribution, like for a instance a spin current or the idea of phonon-magnon scattering at interfaces of NM/FM multilayers, requires either an additional term or the concept of enhanced Gilbert Damping, both of which will be discussed in the concluding section of this chapter.

2.1.6 Ferromagnetic Resonance

The inverse effect of damping can also be achieved under certain conditions. A periodic driving force can be generated that causes the precession to absorb energy if its frequency lies close enough to the FMR frequency, which depends on the magnetic field [9]. When using acoustics, the magneto-elastic coupling results in a change in magnetic isotropy, that exerts a torque on the magnetization, urging the precession on [15].

The equation of the FMR precession frequency was derived by Kittel [19] and now

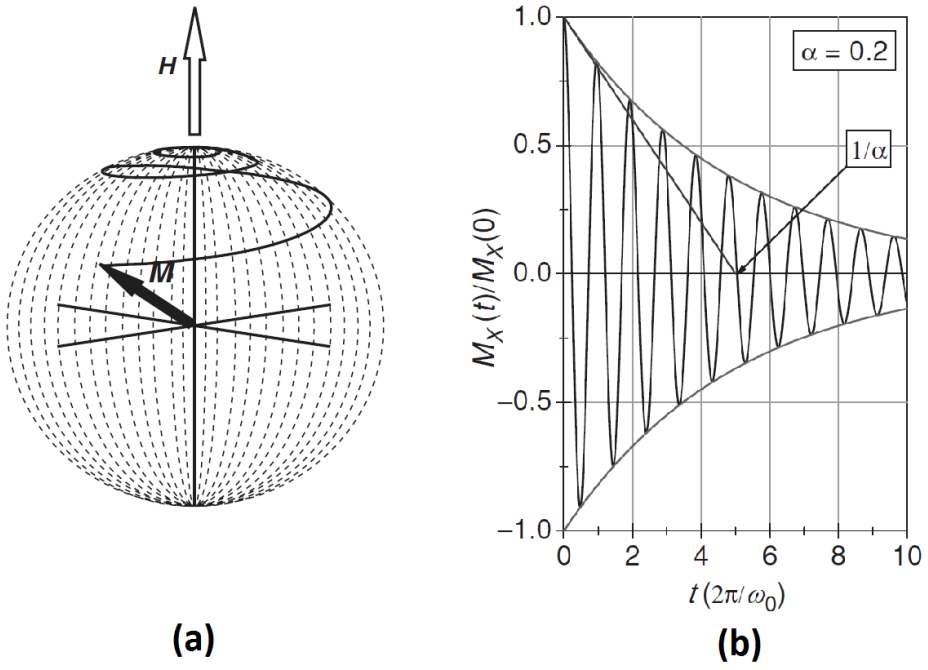

Figure 2.3: *Spiraling motion of the magnetic moment back to equilibrium in 3D (a) and the x component as a function of time, showing the effect of the damping constant (b). Adapted from [6].*

bears his name as the Kittel equation [2, 6]. To derive the condition for FMR, Kittel considered the equation of motion given by the Landau-Lifshitz equation (eq. 2.12) and assumed a static applied field B along the z axis. The full derivation is given in Appendix A.4 and leads to the Kittel equation for FMR frequency:

$$\omega^2 = \gamma^2[B_0 + (N_y - N_z)M][B_0 + (N_x - N_z)M], \tag{2.14}$$

although Kittel himself refers to it in more modest terms as the uniform mode frequency. It describes the lowest energy (k=0) magnon [20]. Higher excitations are also possible (often spoken of in terms of spin wave resonance), but require further theoretical considerations like exchange interactions and the dispersion relation of magneto-phonon polaritons [19, 21]. Since this thesis focuses only on the Kittel mode, no theoretical discussion on higher modes is given.

In the case of a sphere, all components of N are equal and this equation reduces back to the Larmor Precession frequency. However, most experiments, including the one presented in this thesis, are done on thin films [20]. In this case, B lies parallel to the plane of the film and the frequency is given by:

$$\omega = \gamma\sqrt{B_0(B_0 + \mu_0 M)} \tag{2.15}$$

Notice that this equation does not include any exchange interaction as the specimen is assumed to be uniformly magnetized, resulting in the fact that the internal molecular field is always parallel to the applied field [19]. This assumption is sufficient for the experiment that is presented in this thesis. Also, the sample used in the main experiment has no magnetic anisotropies. A modified formula that does include anisotropy effects can be found in reference [22].

The driving force on the precession resulting from the sound waves is incorporated into the traditional LLG equation through modification of the effective field [14, 15] and is shown in A.3, alongside a short discussion on modes that can exist in addition to the Kittel mode.

Figure 2.4 shows experimental results of an FMR experiment conducted on a 50nm Ni film on a soda lime glass substrate. Since in this experiment the sound waves were tuned to precise frequencies, FMR is observed for specific points in field where the precession matches these frequencies. Only the coherent Kittel mode was found in this sample. Standing Spin Waves (see appendix A.3) could have been present, but would not be visible in this experiment's detection scheme, due to the fact that it is only sensitive to modulations of the magnetization perpendicular to the film plane (more details are given in the next chapter). The maximum in the spectrum around

250G corresponds to the surface acoustic wave (SAW) and the maximum around 500G corresponds to the surface skimming longitudinal wave (SSLW).

Since the experimental discovery by Griffiths [19], FMR has grown to an extremely powerful tool. A great variety in magnetic properties of materials can be evaluated using FMR experiments, including: "magnetic anisotropy (or its absence), Curie temperature, magneto-elastic coupling coefficients and relaxation mechanisms" [20].

2.1.7 Spin currents & spin diffusion.

Of prime importance in spintronics is the concept of spin polarized currents (or simply spin currents). One can distinguish spin currents from ordinary currents, if the angular momentum of the electrons making up this current are aligned and preserved [1, 6] (both of which are true only under strict circumstances). Essentially, a spin current is a flow of angular momentum [4].

To examine whether spin will be conserved long enough to speak of a spin current, one must turn to the conduction of the electrons. Electron transport can be ballistic or diffusive. Here, only the latter is discussed, since ballistic transport exists only in the absence of scattering, something that only occurs at extremely low temperatures and short length scales. This thesis focuses on samples larger than the mean free path of the electrons (the length between scattering events) and therefore a discussion on diffusive transport is both appropriate and sufficient. The conductivity σ of a metal is calculated

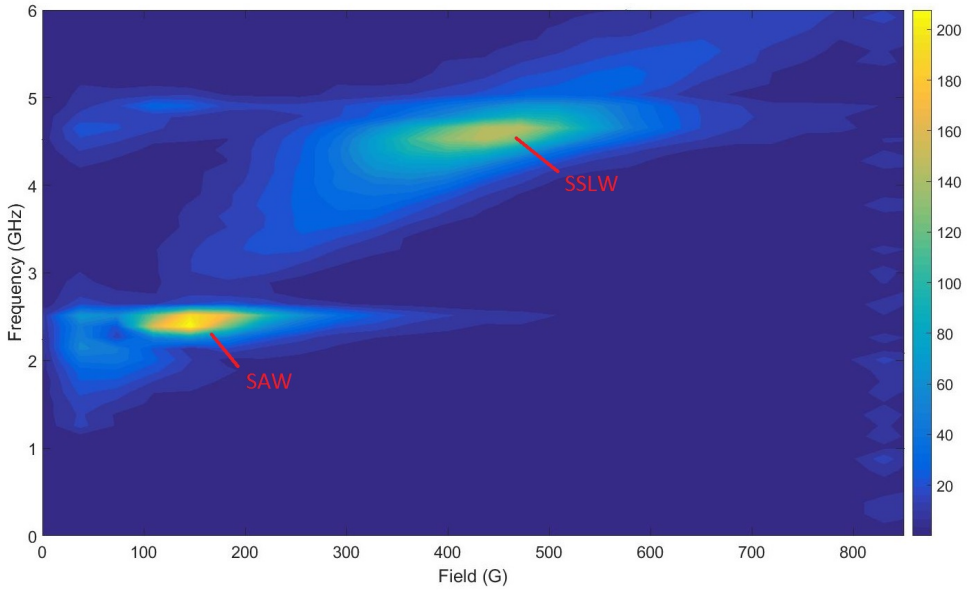

Figure 2.4: *Amplitude of the FMR signal as a function of applied field and frequency of the signal, which follows the acoustic frequency.*

via the free electron model and is related to the mean free path λ as:

$$\sigma = \frac{ne^2\lambda}{m_e v_F}, \tag{2.16}$$

where n is the electron density. The mean free path can also be expressed in terms of the Fermi velocity and the time between collisions (τ) through the standard relation between velocity and distance:

$$\lambda = v_F\tau = \frac{\hbar}{m_e}(3\pi^2 n)^{1/3} \tag{2.17}$$

An electron can be subject to as many as 100 scattering events before it is flipped and loses its angular momentum information, i.e. $\tau_S = 100\tau$ (see Figure 2.5). The spin

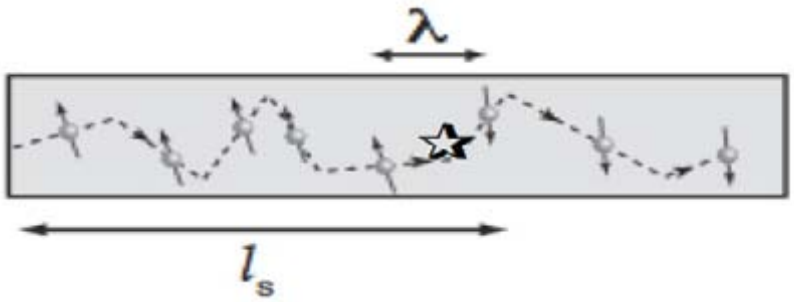

Figure 2.5: *Diffusive electron transport in metals. Adapted from [6].*

diffusion length l_S can be calculated using this information and the random walk expression, since the conduction is considered to be diffusive. The diffusion constant of the electrons is given by:

$$D_e = \frac{\sigma}{e^2 N(E_F)} = (1/3)v_F\lambda, \tag{2.18}$$

making

$$l_S = \sqrt{D_e\tau_S} = \sqrt{\frac{1}{3}Q\lambda^2}, \tag{2.19}$$

where Q is the ratio between τ and τ_S (typically 100).

For copper, the values of the conduction and λ are the same for both up and down spins. However, for some ferromagnets the scattering events are different for both as the density of states is spin split. For Ni, for instance, the spin down electrons can be scattered into empty 3d states that are not available for spin up electrons, as can be seen in Figure 2.6. This causes that λ for spins up and down differs by about a factor of 5 in Ni.

Since the spin diffusion length is such an important parameter in spintronic re-

search, a lot of studies have quantified it for various materials. Table 2.1 lists the values found in several metals at room temperature that are important for this thesis.

Material	l_S (nm)
Ni	10
Cu	200
Pt	1.2-3.7
Ti	13.3

Table 2.1: *Spin diffusion lengths of several metals at room temperature, taken from references [3, 6, 23, 24]*

Decreasing the temperature will increase l_S because fewer phonons means fewer possibilities for scattering events [23, 25].

2.1.8 Spin Wave pumping

As with ordinary currents, spin currents are driven through the generation of a so called spin voltage [1]. This voltage can be generated in two different ways, one of which is spin wave pumping [26, 27].

Spin wave pumping describes the flow of angular momentum from a ferromagnetic metal (FM) into an adjacent normal metal (NM) [26]. This can be driven in several ways, all of which depend on exciting non-equilibrium magnetization dynamics [11]. FMR is one of those ways, driving spin currents through magneto-elastic coupling. This is also called acoustic spin pumping as it relies on sound waves [28]. Essentially, it can be seen as a resonance extension of the spin Seebeck effect, which is described in Appendix A.5.

When a FM/NM junction is formed, the spin populations on either side change on a length scale of the spin diffusion length in the respective materials [6], as depicted in Figure 2.7. This is called spin accumulation. In equilibrium, these changes are quite small. However, when spin currents start to play a role, this becomes a much greater deal.

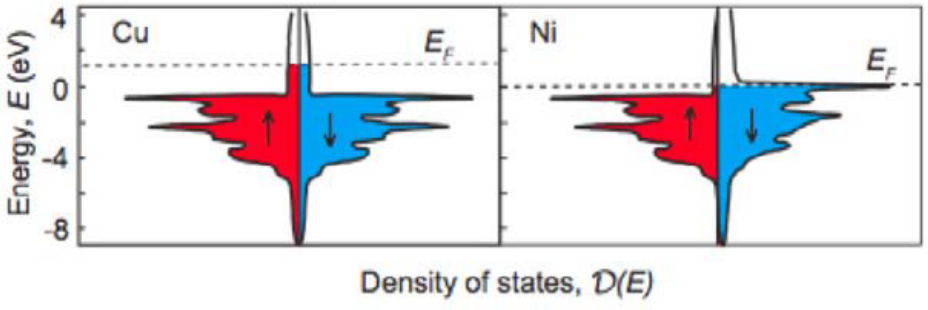

Figure 2.6: *Density of states in Cu and Ni near the Fermi level. Adapted from [6].*

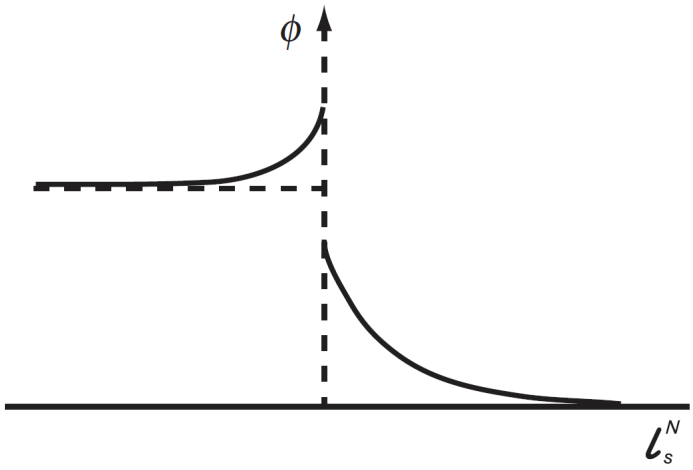

Figure 2.7: *Changes in spin population within the FM (left) and NM (right) near the interface. Adapted from [6].*

In FMR experiments, the picture of spins up and down is somewhat inadequate, as the pumped spins are not simply polarized but still precess as they did in the ferromagnet, until they are relaxed through the usual mechanisms (see previous sections) [2]. Figure 2.8 paints this picture. The current can flow from the ferromagnet into the

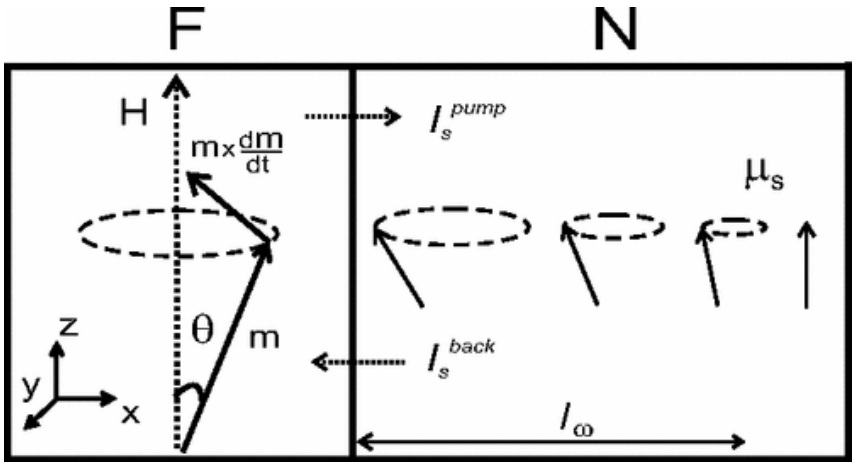

Figure 2.8: *FMR spin pumping in a ferromagnetic (F)- normal metal (N) junction. Adapted from [2].*

normal magnet, but can also return. Interestingly, it is perfectly common that in terms of charge both currents are equal, resulting in 0 net charge current [11]. However, it is still possible to create a net spin current, through the fact that spins are polarized when transferred from the ferromagnet into the normal metal and randomized upon return. If the normal metal dimensions exceed the diffusion length, it will act as a good spin sink and cause additional damping in the FMR of the ferromagnet [29].

The concept described above can also be used to achieve the opposite effect, actually depositing angular momentum in a ferromagnet through direct injection of a

spin current [12]. This is called spin transfer torque and is the subject of quite some research, as it is even more effective at applying torque to a nanosystem than magnetic fields from currents [6].

Incorporating both spin transfer torque and spin wave pumping into the LLG equation (eq. 2.13) can be done in different ways, depending on additional effects. An et al. employ an additional term that incorporates spin transfer effects and influences from their injected current [3]. As our experiment relies on FMR, not on current, this additional term will not be needed. Adachi et al. added a separate term that originated from the s-d exchange interaction (J_{sd}) and accounts for spin transfer across the interface and split the effective magnetic field in the static (H_0) and dynamic (h_{ac}) components [11]: Another method was put forth by Barati et al. separating all possible torques on the magnetization [17]: However, all of these equations are unnecessarily extensive. It is far more common to model spin currents solely on a symptomatic basis, making use of the superposition of the original intrinsic damping parameter α and the extrinsic damping α' [6, 13, 30, 29]:

$$\frac{dM}{dt} = -\gamma M \times H_{eff} + (\alpha + \alpha')M \times \frac{dM}{dt} \tag{2.20}$$

The concept of an enhanced Gilbert factor makes measuring damping effects in this experiment very easy. One must only ensure that a good reference sample is present. By examining the damping on a reference sample and comparing it to others, the effect of spin currents, or absence thereof, can be identified and even quantified.

Several FMR experiments have been conducted, most utilizing the inverse spin-Hall effect that is a result of the spin currents. The approach in this thesis is different in the sense that the investigation of the enhanced damping is done directly on the magnetization dynamics.

2.2 Light & matter interactions

The experimental approach will rely on all optical excitation and probing. It is therefore paramount to treat some rudimentary notions on interactions between light and matter.

2.2.1 Birefringence

Crystals have anisotropies [9]. Because of the periodicity of the atoms, not all directions are equal. This can have many consequences, but here we restrict the discussion to one particular effect that arise when the crystal is optically anisotropic. Because of the

optical anisotropy, light that is polarized in different ways may experience different indices of refraction and the crystal is said to be birefringent [31].

Birefringence is a result of the fact that light propagates in a medium through the excitation of the electrons via the electric field of the wave. The electrons send out the refracted wavelets and the wave propagates on. Since the excitational movement of the electrons depends (in the classical picture) on the force that binds them to the atom, a directional dependence of this force will result in a difference in natural frequency of the electrons along that path from one another, which results in different propagation speeds for electromagnetic waves. Since the direction of the electric field is coupled to the polarization, two differently polarized waves travelling along the same path will still attain a difference in propagating speed and, therefore, index of refraction.

Birefringence drives several applications. In our experiment we use one of them, called a Wollaston prism. Figure 2.9 shows its workings. The incoming beam is trans-

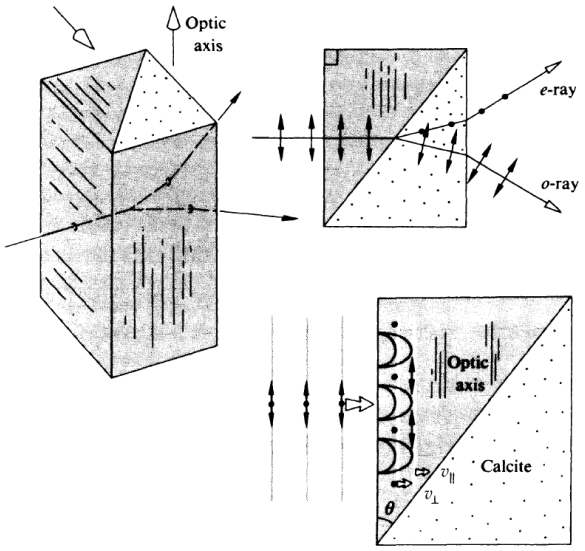

Figure 2.9: *Geometry and working principle of a Wollaston prism. Adapted from [31].*

mitted straight into the crystal, but encounters a tilted interface halfway through the prism. The difference in index of refraction of the two polarization directions that make up the beam causes the beam to split into two beams that are refracted at different angles. The beams are then transmitted back into the air and refract away in opposite directions, creating even more spatial separation between them.

2.2.2 Faraday effect

The main tool that the detection scheme in the experiment of this thesis uses in the direct probing of the magnetization is the Faraday effect. It was discovered in 1845 by the man whose name it now bears [31]. It is the rotation of the polarization of light

that is transmitted through a magnetized piece of material. It is the result of circular birefringence. Right and left circularly polarized light beams traverse the material at different speeds. Since linearly polarized light is comprised of a superposition of both, the net effect of one lagging the other is a rotation of the angle (which depends on the phases of the circular components).

The change in polarization angle depends on the magnetization of the sample and the optical path length (not on the external field) [6]:

$$\Theta_F = k_v \int \mu_0 M \cdot dl = k_v B l \tag{2.21}$$

The latter equality holds for a material that is uniformly magnetized along the path of the light. The dot product in the first equality puts forth two notions of importance. Firstly, the Faraday effect in non-reciprocal, meaning that when a beam is passed through a material, reflected and passed again along its original path, the resulting change in angle will not be zero, but double the single pass value. This is because, although the propagation of the beam is now anti-parallel to the magnetization, the helicity changes upon reflection as well, resulting in a double negative. Secondly, it means the Faraday effect is sensitive only to the component of the magnetization in the direction of light propagation. When using the Faraday effect as a probing mechanism, it is paramount to consider this when designing a suitable set-up.

Chapter 3

Experiment

In this study, ultrafast TG spectroscopy was utilized to study the effect of the thickness of several underlayers on the acoustic and magnetic response of Ni films to specifically tuned acoustic waves. This chapter takes the reader through a description of this method, sample preparation and some background knowledge necessary to understand the experiment.

3.1 Sample preparation

The samples were prepared in a Temescal FC2000 e-beam evaporator. Deposition was performed in vacuum at approximately 10^{-7} Torr.

Figure 3.1 shows a schematic depiction of the sample composition. The samples

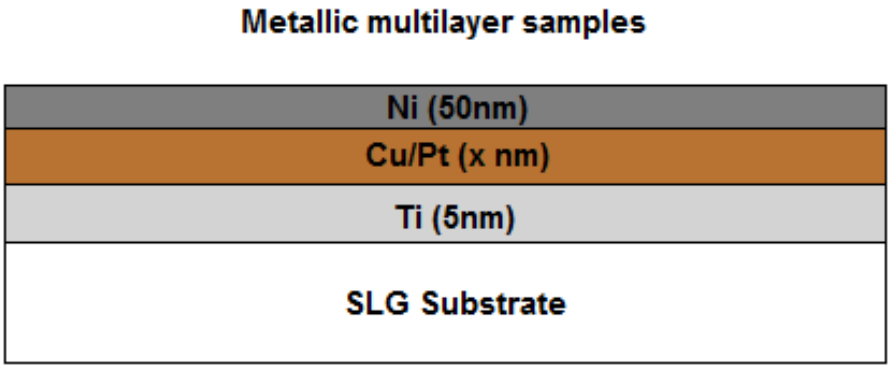

Figure 3.1: *Side-view of the samples. X was varied from 0-50 nm for Cu and 0-30 nm for Pt.*

were made on soda lime glass substrate of 1mm thickness, which were first coated with a 5nm Ti layer to support adhesion of the underlayer. Subsequently, an underlayer of either Cu or Pt was deposited, varying the thickness for the different samples. The samples were completed by coating of a Ni film of (fixed) 50nm thickness. All

steps were performed sequentially without breaking vacuum, to prevent the forming of oxidation layers on anything but the Ni. The sole exception was a set of two additonal samples of 12nm and 25nm Pt that were exposed to air before the Ni was coated on top to investigate possible differences as a result of an oxidized underlayer.

The thickness X of the underlayers for the Cu samples consisted of the following set: $\{0, 3, 6, 12, 18, 25, 50\}$(nm), where 0nm represents the Ti-Ni reference sample. Due to the fact that Pt transmits less light from the probe beam than Cu, the thicknesses of said layer were set at x= $\{0, 3, 6, 9, 12, 16, 20, 25, 30\}$(nm). The accuracy with which the evaporator can achieve this lies within the range of a few Angstrom.

After preparation, the samples were exposed to air for a significant amount of time. Oxidation of the Ni is considered to have occurred equally for each sample.

3.2 Pump-probe experimentation

Since the magnetization dynamics that are to be studied here precess at frequencies in the order of GHz, a technique that can measure with sub nanosecond resolution and precision is needed to achieve the required accuracy [32]. To this end, we make use of the so called pump-probe experiment.

The pump probe principle relies on the generation of very short pulses of light and displacing them from each other in time. The first pulse is used to bring the system out of equilibrium. The second pulse probes the dynamics, by changing the temporal separation of the two pulses and measuring at each point in time. By ensuring that the pump samples a larger area than the probe, edge effects are mitigated or absent.

Figure 3.2 shows an example of a pump probe set-up. A (modelocked) laser comes

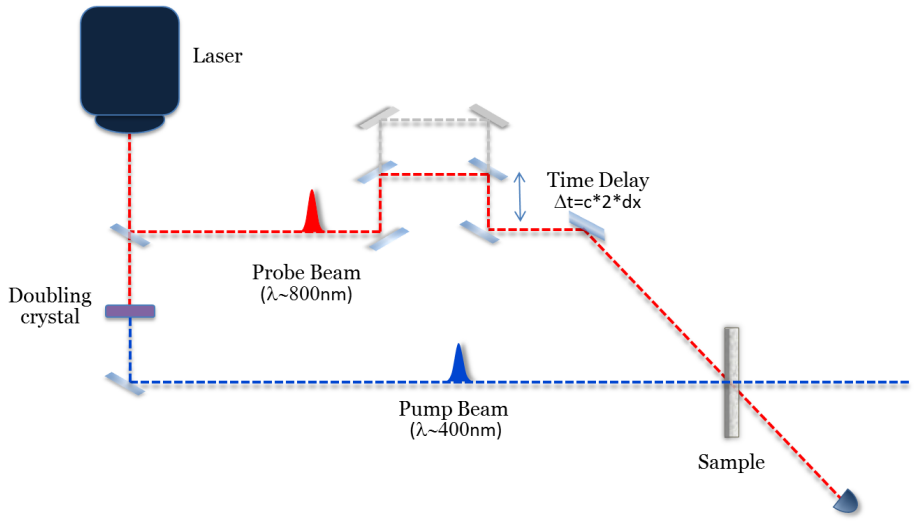

Figure 3.2: *Simplified representation of a traditional pump-probe set-up.*

in at a 1kHz repetition rate. The beam is split into two parts, of which one becomes the probe beam and the other the pump. The pump can be converted to half the wavelength utilizing a nonlinear crystal. This allows for chromatic filtering at the detector. By varying the time delay between the incoming beams, different snapshots can be taken of the real time dynamics. Together, these snapshots create the time evolution of the samples response to the pump excitation. It is noteworthy that it must be ensured that the system returns to equilibrium between excitation pulses. However, this is easily achieved.

Utilizing pump probe methods offer various advantages [33]:

- High temporal resolution
  Because the temporal resolution is directly limited by the temporal pulse length, the usage of ultrashort pulses (in the fs range or, by exception, even lower) ensures that the temporal resolution is incredibly high. Furthermore the pump-probe technique does not call for equipment to run on the same timescales.

- Short spatial pulse length
  The pulse length can be as short as a few micrometers, making this technique useful for imaging.

- High peak intensity
  Since the laser light is pulsed rather than continuous, extremely high peak intensities can be achieved without increasing the average power. This has several advantages, among which is that it facilitates the frequency doubling.

3.3 Transient Grating Spectroscopy

In addition to the traditional pump-probe experiments, a technique called TG photoacoustics has been developed [34]. This method uses interference of light to create a periodic excitation of the sample, in contrast to the simple monotonic excitation described in the previous section.

In TG experiments, two pump beams are used instead of one. They are spatially and temporally overlapped at the sample to create an interference pattern [35]. Calculating the resultant intensity profile becomes fairly straightforward when considering the electric field. Following the superposition principle, the resultant intensity, I, at the sample is given by [31]:

$$I = (E_1 + E_2)^2, \quad where \quad E_n = E_n e^{(\omega t - \mathbf{k_n} \cdot \mathbf{x})} \tag{3.1}$$

Looking at Figure 3.3, which depicts the standard situation at the sample, it is easily seen that the k vectors of the two pump beams differ in only one dimension, where they are opposite in sign and equal in magnitude (by design). In addition, the two pump beams are of equal intensity. Taking these boundary conditions, I takes the form:

$$I(x) = (Ee^{i\omega t}(e^{i(k_z z + k_x x)} + e^{i(k_z z - k_x x)}))^2 \quad = E^2 e^{2i\omega t}(e^{2i(k_z z + k_x x)} + e^{2i(k_z z - k_x x)} + 2e^{2ik_z z})$$

Using Euler's formula:

$$I(x) = E^2 e^{2i\omega t} 2e^{2i(k_z z)}(2 + 2cos(2k_x x)) \tag{3.2}$$

Defining z=0 and t=0 at the crossing at the sample and using the double angle rule, one arrives at:

$$I(x) = 4E^2 cos^2(k_x x) = I_0 cos^2(k_x x) \tag{3.3}$$

The crossing of the two beams create an intensity pattern that modulates between I_0 and 0, creating hot and cold regions that precisely define the amount of intensity available for absorption. The periodicity is dependent on k_x, which is a quantity easily controlled by the crossing angle of the beams. From the geometry in Figure 3.3 it is obvious that:

$$k_x = ksin(\theta) \tag{3.4}$$

Filling this in and noticing that the periodicity of the excitation should equal π (the periodicity of cos^2):

$$\Lambda ksin(\theta) = \pi \tag{3.5}$$

Therefore we can write:

$$\Lambda = \frac{\lambda}{2sin(\theta)} \tag{3.6}$$

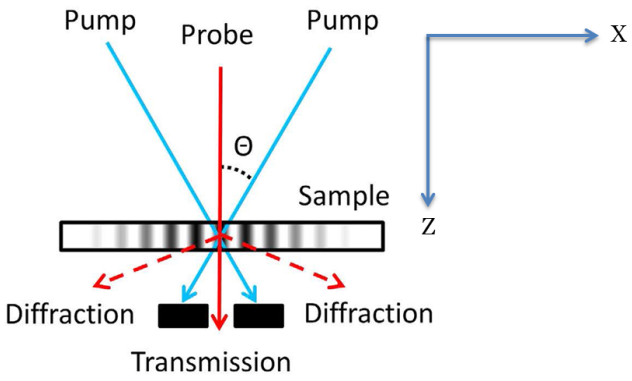

Figure 3.3: *Interference pattern of the pump beams overlapping at the sample position. Adapted from [35]*

Here λ is the wavelength of the pump beam. The equation is most often written in terms of the scattering wave vector magnitude q [36, 37]:

$$q = \frac{4\pi sin(\Theta/2)}{\lambda} \tag{3.7}$$

Here Θ is now the full angle between the two beams.

Since the creating of hot and cold regions also creates dilation and contraction in the same periodic manner, acoustic waves with the same wavelength are automatically produced via thermo-elastic interactions. Furthermore, the excitation is primarily damped via thermal diffusion, which follows the well-known (isotropic) heat equation [38]:

$$\frac{\delta u}{\delta t} - \alpha \nabla u = 0 \tag{3.8}$$

The readers attention is now directed back to the original solution to the excitation pattern, which satisfies this equation. Therefore, the heat diffusion will not change the shape of the heat distribution.

This fine control over the periodicity and the ease of varying it allows a wide array of experiments to be performed. The TG method has been utilized to determine elastic properties, residual stresses, thermal diffusivity, ferromagnetic resonance and film thickness [32, 36, 37, 39, 40, 41].

The TG method has one final problem that has been ignored in the calculations. Due to the limited temporal extent of the beams, achieving the proper interference pattern happens only at the very center where the beams cross. Since the wave fronts propagate at different angles, their overlap is incomplete. A simple solution exists to this problem, which shall be discussed in the next section.

3.4 Set-up

The experimental set-up is shown in Figure 3.4 The problem of the different angles of the wave fronts is overcome by imaging a diffraction grating directly onto the sample using a single pump beam. Another advantage of this with respect to simply overlapping two beams is that temporal and spatial overlap are guaranteed as there is no difference in path length to be taken care of. Additionally, by making use of a translatable diffraction grating with different grating periods available, tuning the periodicity of the excitation becomes a very quick and simple process.

The time delay between probe and pump is varied by use of a delay stage that features a retro reflector. The pump is chopped at a frequency of 272KHz, so that the instrumentation can easily separate the signal that is due to the pump by tuning to this

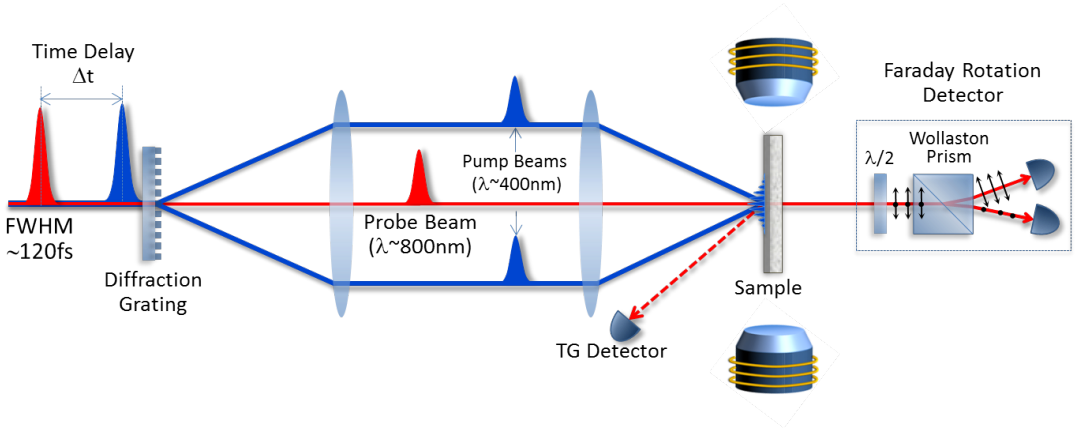

Figure 3.4: *Experimental set-up.*

frequency. Around the sample, a magnet is placed at an angle of roughly 15 degrees with respect to the horizon for maximum signal. Detectors are placed at two locations. The TG detector measures the diffraction of the probe beam due to the periodic modulations on the sample surface, caused in this case by the SAW [32]. The second place features two detectors and lies along the central axis. A Wollaston prism separates the two directions of polarization present in the beams and sends each to one of the detectors. Since the magnetic precession causes the polarization of the passing beam to change as a results of the Faraday effect, actively tracking the difference in light hitting the two detectors measures the relative magnetization directly and in real time.

3.5 The importance of high fluence

The experiment above is subject to a noteworthy, but surmountable, concern. The equilibrium vector of the intrinsic magnetic moment lies with in the plane of the sample, at approximately 15 degrees with respect to the horizon (and thus to the k-vector attributed to the excitation). After excitation, the magnetic moments of the electrons will precess around this direction as depicted in Figure 3.5. If the x,y plane is defined such that it lies parallel to the sample surface, H lies within this plane only. The magnetic moment of a single particle will therefore have a z component proportional to a sinusoidal function in time. It is exactly this z component that causes the Faraday effect on the probe beam and therefore what the detectors at the end of the set-up are sensitive to [35]. However, the probe beam samples a spot size of a few hundred micrometers in diameter and will therefore sample several wavelengths of the excitation pattern, which in this experiment is only roughly 1.1μm. Over one period of the excitation all phases of oscillation are excited equally, meaning that for every positive z-component of the magnetization, there is another negative component of equal magnitude at any given

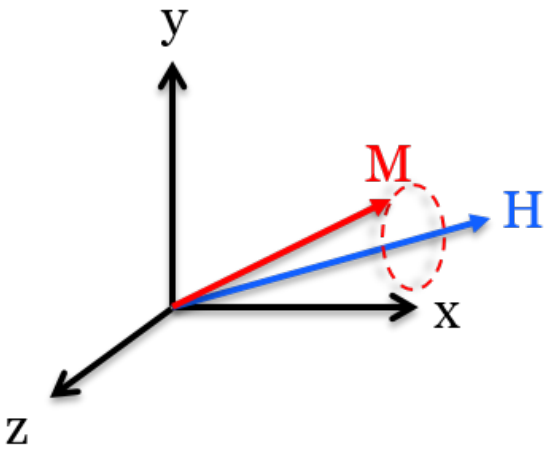

Figure 3.5: *Precession of the magnetic moment around the applied field after disrupting equilibrium.*

time, averaging the net magnetization along the z-axis to 0 over one wavelength, as can also be seen by looking at Figure 3.6 (a). Nevertheless, when fluence is high enough, temperature causes demagnetization of the sample in the hot regions as is shown in Figure 3.6 (b)-(e). This demagnetization occurs as the hot regions approach (or surpass) the Curie temperature. Because the phase between the magnon and elastic wave are strongly correlated, a very specific phase is demagnetized, as depicted in Figure 3.6 (c). By selecting the optimum fluence of the pump laser, one can in this way maximize the signal at the point where one direction of the magnetization is erased, whereas the other remains largely untampered with. It is noteworthy that, while this phase of the magnetization precession is erased, the sample remains slightly magnetized along the applied magnetic field (in correspondence with Figure A.2), but the Z component is equal to 0.

3.6 Previous measurements on Ni

FMR and/or spin pump measurements on Ni samples (or samples where Ni fulfills the role of ferromagnet) have been widely done [14, 32, 35, 42, 43, 44], in part because its response is quite high in amplitude and the damping is reasonably low. One study that is of particular note is that performed by Walowski et. al [30]. Walowski et. al studied the intrinsic damping of Ni in addition to the added effect of other materials by varying the Ni thickness and comparing the results. They found that for layer thicknesses below 10-15nm, extra damping occurred in the Ni samples with an added layer, pointing towards the presence of spin wave pumping in their experiment. They

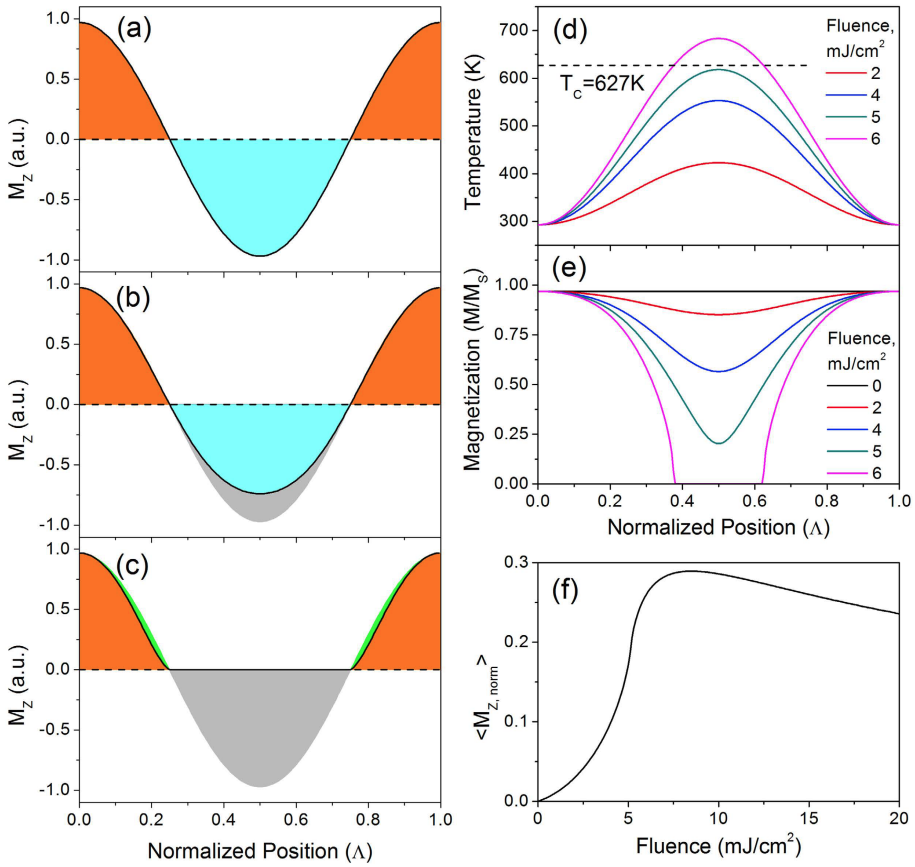

Figure 3.6: *long wavelength magnetostatic spin wave samples all phases of precession orientation and thus the out-of-plane component, Mz, averages to zero over the full period. (b) A spatially periodic thermal excitation suppresses the magnetization, and correspondingly Mz. Under low fluence conditions, one phase of precession is suppressed resulting in a net magnetization. (c) Under high fluence conditions, more than half of the period demagnetizes. (d) Temperature profiles after the equilibration throughout the thickness of the 40 nm thick film (corresponding to t = 35 ps after the excitation) and corresponding magnetization values (e), normalized to the saturation value at T = 0 K. Due to the spatially dependent suppression, the detected magnetization is a fraction of the magnetostatic wave amplitude. The sensitivity dependence of the detection scheme upon fluence is shown in (f). Figure and caption reproduced from [35].*

also found that when they increased the Ni thickness further, the difference in terms of damping between the reference Ni sample and those with overlayers disappeared, as can be seen in Figure 3.7. This result shows that spin pumping occurs for Ni films below a certain thickness, that is by no means arbitrary. Although not stated by Walowski et. al, the disappearance of additional damping occurs around the time where the Ni film thickness exceeds the spin diffusion length, which equals 10nm [6]. Since their experimental set-up featured the Kerr-effect as a tool and the excitation was superficial, the detection scheme was only sensitive to whatever happened on or very near the surface. Spins precession that would move away from that position would never reach the spin sink, since it would lose its well defined angular momentum in the Ni

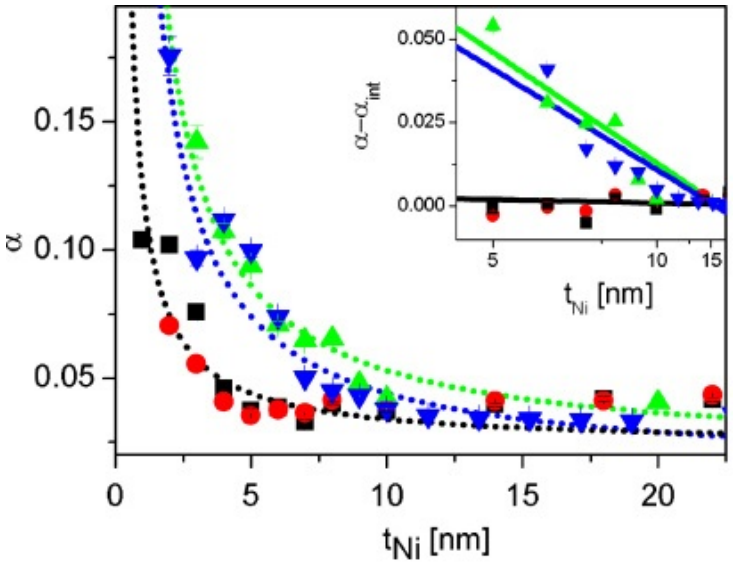

Figure 3.7: *Gilbert damping factor α as a function of Ni thickness for different overlayers. Figure reproduced from [30].*

itself.

The experiment treated here builds on this, but moves on to a detection scheme based on transmission, that therefore probes the entire sample. Moreover, FMR is used as a driving force. The Ni film thickness is kept constant and far larger than the spin diffusion length. This study aims to find whether spin pumping still occurs near the interface and whether the behaviour of the spin sink can be identified as its thickness comes closer and closer to the spin diffusion length. The data is analyzed using fitting to a function similar to that used by Walowski et al.:

$$A(1 - e^{\frac{-t}{\tau_1}})cos(f2\pi t - \phi)e^{\frac{-t}{\tau_2}} - C \tag{3.9}$$

The first term is a constant, the second term accounts for the rising time τ_1 in the signal, the third term accounts for the frequency of the wave, f, and its initial phase, ϕ and the final term gets rid of any remaining background signal on our detectors, that might stem for slight misalignment or another source. All variables, except for t, are used as fitting parameters.

Chapter 4

Results & analysis

In this section the results of the TG spectroscopy measurements on Ni, Ni-Ti, Ni-Cu-Ti and Ni-Pt-Ti are presented. The diffracted probe beam was measured in reflection, as well as the difference of the signal in the two Faraday detectors.

4.1 Acoustics

Because the driving force in this experiment depends on the generated sound waves, it is important to investigate the acoustic response of every sample. In order to say something about spin diffusion one has first to examine whether other effects play a role. The reflection TG detector is sensitive to the surface of the sample and therefore shows the behaviour of the SAW. The SSLW can only be examined in transmission. However, the samples proved to be to optically dense to leave enough signal. Therefore the acoustic analysis is focused on the SAW only.

The acoustic signal is shown in Figure 4.1. Upon comparing the signals one can see that for the Pt samples all acoustic signals show the same behaviour in terms of damping, while for the Cu samples this is not true. Cu, instead, seems to damp the acoustic signal more and more with increasing thickness. This can be understood by looking at the underlying mechanisms. The sounds waves are produced by the periodic heating of the sample. The prolonged existence of the wave is dependent on the ability of the film to retain this profile. However, upon examining the heat conductance of Cu (see table 4.1), it is immediately clear that it might impact the heat distribution in the sample, since it so much bigger than that of Ni. This is something that has to be taken into account when examining the magnetic response of the Cu samples. For thin copper layers the effect is minimal, as the layer is not able to absorb too much of the heat. However, for increasing thickness, it becomes more and more effective as a heat sink. Following the same argument it is clear why this is not an issue for the Ti and/or

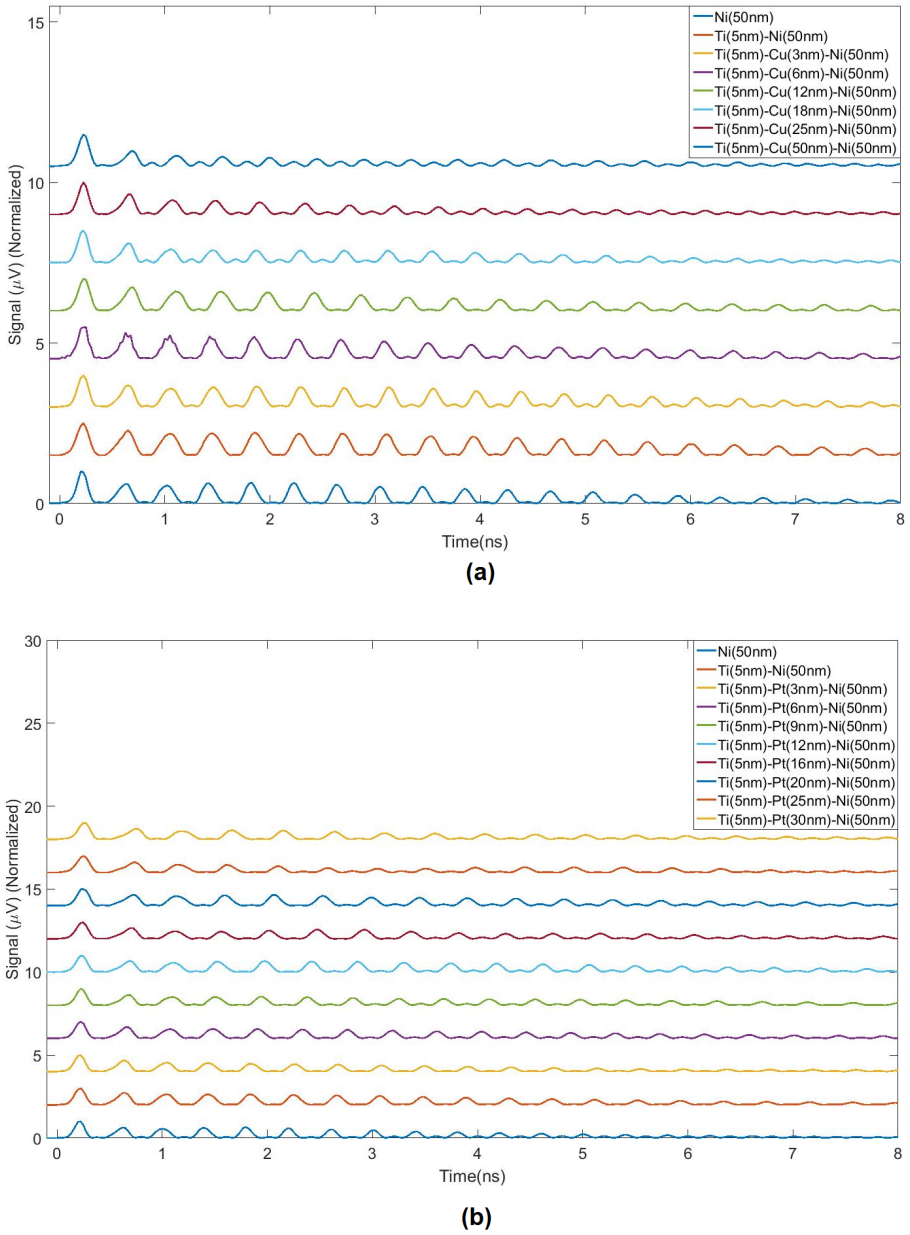

Figure 4.1: *Time traces of the diffracted probe beam intensity due to SAW for several metallic multilayers normalized to one. (a) shows the measurements for the Cu samples and (b) for the Pt samples together with the reference samples.*

Pt, since both have a heat conductance below that of Ni.

The second thing that one can see in the time traces is the downward shift in frequency for both the Cu and Pt samples with increasing thickness, which is also presented more clearly in Figure 4.2. The behaviour is seen most clearly in the shift of the right hand peaks, which are a result of the second harmonic of the signal, as evidenced by the fact that they are exactly twice the frequency of their original counterparts as well as the fact that it can be clearly observed as intermediate peaks in the time traces

Material	Heat conductance $(W/m \cdot K)$	K (GPa)	G (GPa)	$\rho(g/cm^3)$
Ni	92	180	86	8.897
Cu	401	140	42-55	8.932
Pt	73	230	61	21.45
Ti	22	105.6	43.5	4.51

Table 4.1: *Heat conductances, bulk moduli (K), Shear moduli (G) & densities (ρ) of several metals at room temperature, taken from [45].*

(Figure 4.1) This is as expected. The sound velocity (and therefore its frequency, since wavelength and deformation mode are kept constant by virtue of the set-up) depends on the elastic constants of the material. For a longitudinal wave in an isotropic bulk material, the velocity is given by [46]:

$$v_L = \sqrt{\frac{K + \frac{4}{3}G}{\rho}}, \tag{4.1}$$

where ρ is the density of the material, K is the bulk modulus of the material and G is the Shear Modulus. This formula holds for the SSLW, but not for the SAW, as the SAW is a Rayleigh wave and therefore depends on both the longitudinal wave velocity and the shear wave velocity, which is given by:

$$v_S = \sqrt{\frac{G}{\rho}} \tag{4.2}$$

The Rayleigh wave velocity V_R depends on these velocities via the Rayleigh wave equation [47]:

$$[2 - (\frac{v_R}{v_T})^2]^2 = 4\sqrt{[1 - (\frac{v_R}{v_L})^2}\sqrt{1 - (\frac{v_R}{v_T})^2}, \tag{4.3}$$

which can either be solved numerically, or by the usage of an approximate formula that knows several variations.

For thin films, especially those comprised of more than one material, matters are somewhat more complicated than for bulk materials, because the film can no longer be approximated by an infinite half-plane and wave guiding occurs. The SAW typically has a penetration depth around its wavelength, which in our case is set to $1.1\mu m$. Therefore, it samples all layers and even part of the substrate. With increasing thickness of a layer, the acoustic response of the SAW will be pulled more and more to the velocity in that material, instead of that of the Ni and glass substrate (which are similar) [48]. Due to the fact that the Rayleigh wave velocity is lower in the Cu and Pt layers, because their moduli divided by their density are much lower (see table 4.1), the total velocity decreases with increasing thickness of the layers.

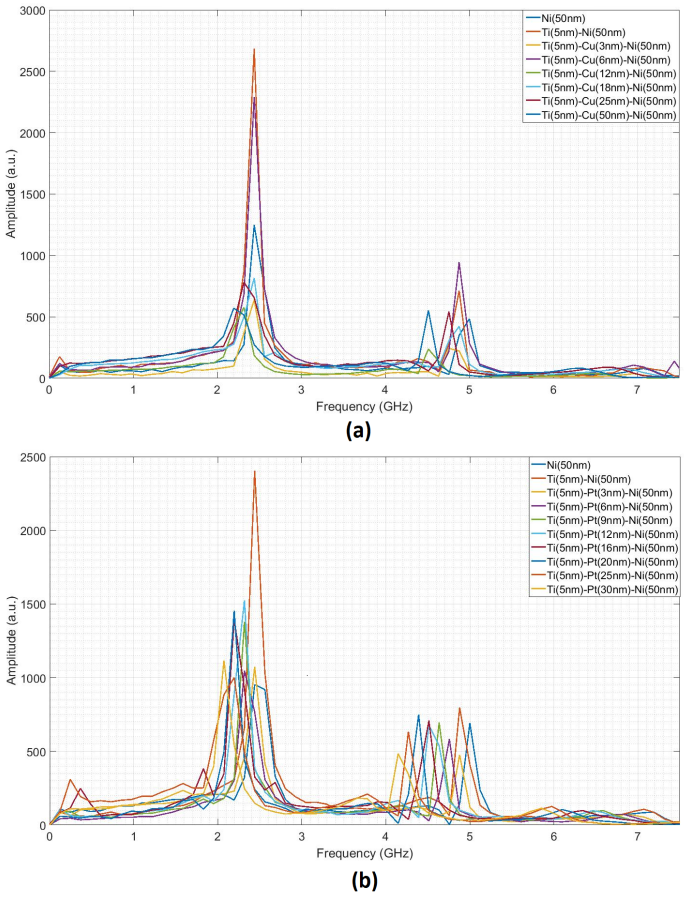

Figure 4.2: *Fourier transforms of the SAW signal for several metallic multilayers. (a) shows the measurements for the Cu samples and (b) for the Pt samples together with the reference samples. The peak on the right is due to the second harmonic.*

4.2 Magnetic field dependency

To identify what FMR modes are present and what their resonance frequencies are, a field dependent scan is done, taking time traces using the Faraday detection scheme at different applied fields. The result is then Fourier transformed to give 2D graphs, of which two are shown in Figures 4.3 and 4.4. Comparing these to the Ni reference sample (Figure 2.4) one can already see that the amplitude on resonance of the Fourier transforms have gone down after introducing the Ti layer and are even further reduced by the 50nm Cu layer. This can be the result of a lower amplitude in the time traces, or a faster damping of said signals, the latter of which might indicate spin wave pumping. However, this is not expected to be the result of the Cu layer, because 50nm is still far below the spin diffusion length.

Another thing that strikes the eye is that the SAW seems more prominent in the Ni sample, but has almost died out in the 50nm Cu sample, whereas the SSLW, while damped, is less affected. This is explained by considering the nature of the two waves.

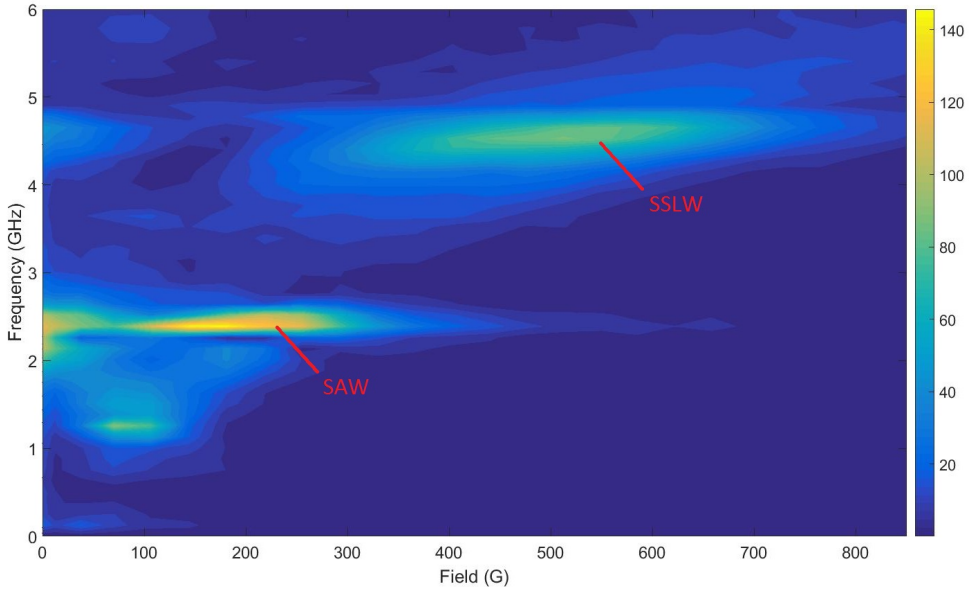

Figure 4.3: *Field dependence of the Faraday signal of Ti(5nm)-Ni(50nm) in frequency space.*

The SAW is highly delocalized, whereas the SSLW behaves as a bulk longitudinal wave. The SAW is therefore more susceptible to the effect of the additional layers. The fact that this same behaviour was not observed for the platinum layer, supports the theory that this is the result of the acoustics, rather than the magnetization, as platinum does not influence the acoustics, in terms of damping.

Finally, the same frequency shift that was seen in the acoustics signal is also observed here. This is in agreement with the theory, as the oscillation is a resonant process and should follow the sound waves in terms of frequency.

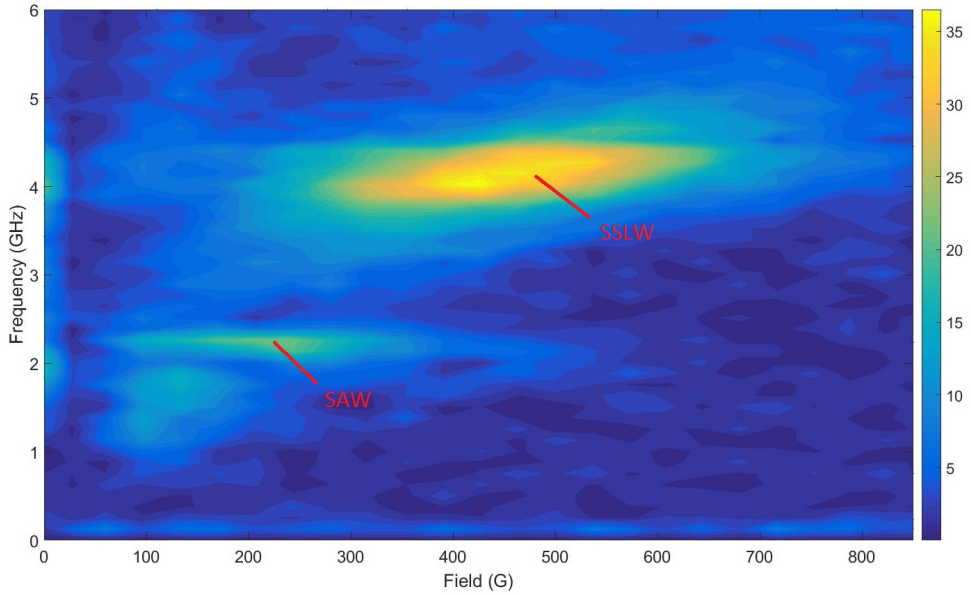

Figure 4.4: *Field dependence of Ti(5nm)-Cu(50nm)-Ni(50nm) in frequency space.*

4.3 Behaviour at FMR conditions

Because the amplitude of the Fourier transform depends on both amplitude and damping, single scans were taken under resonance conditions, to examine the damping present in the signals (see Figures 4.5-4.8). The traces were then fitted, following equa-

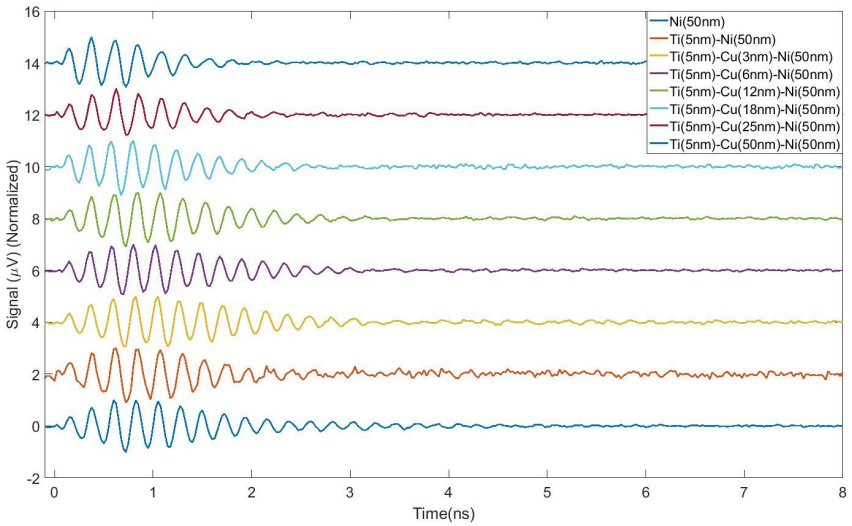

Figure 4.5: *Time traces of Cu samples at SSLW resonance.*

tion 3.9. The results are shown in Figures 4.9-4.12.

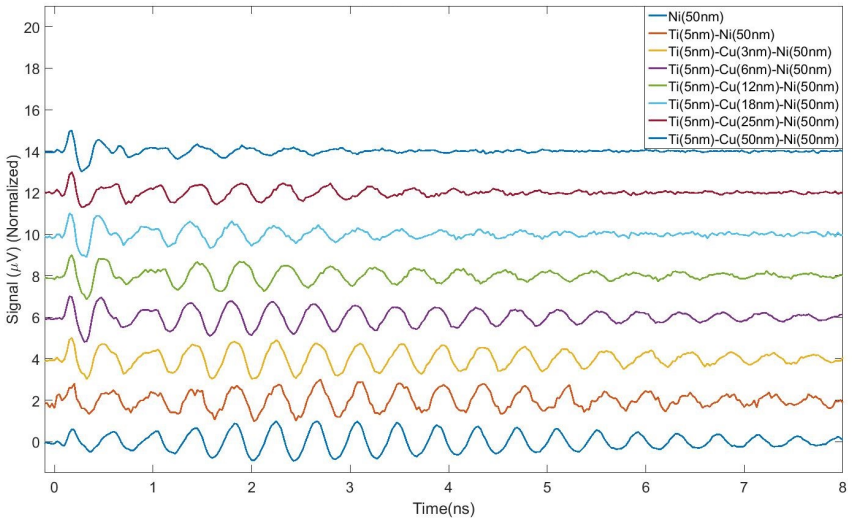

Figure 4.6: *Time traces of Cu samples at SAW resonance.*

For the SAW (Figure 4.9) the Cu samples show a clear decline in damping time with increasing thickness, which constitutes faster damping. However, since similar behaviour was also seen in the acoustics channel, one cannot draw conclusions regarding magnetic mechanisms that might or might not be involved.

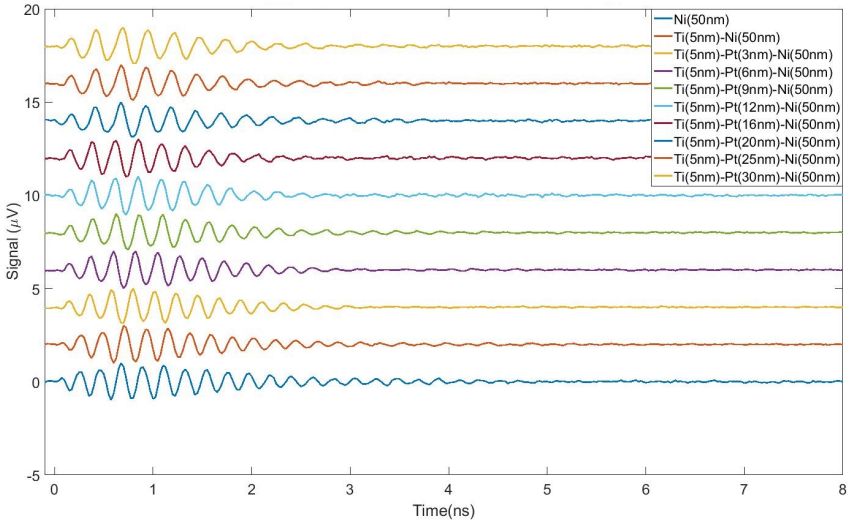

Figure 4.7: *Time traces of Pt samples at SSLW resonance as a function of underlayer thickness.*

Based on the spin wave pumping theory and the previous evidence of the SAW being able to drive this [4], one would have expected the samples with Ti and with Ti and Cu to exhibit lower damping (so higher damping time) than the Pt samples, as for the latter we are above the spin diffusion length and we are below that of Ti and Cu for the respective layer thicknesses. In addition, the graphs are expected to go down with increasing thickness up to the spin diffusion length, since this constitutes the point at which all the spins diffuse in the spin sink and additional thickness will therefore change nothing. At that point all that matters is the scattering at the interface, which determines the efficiency of the spin pumping. The expected behaviour was not observed in the purest manner, partially because for the Cu samples the driving force differed from that of the platinum samples. Therefore, whether or not the increase in damping of the Cu samples is a result of spin wave pumping is u for debate, although the absence of a plateau is well within the theory as the spin diffusion length of 200nm was not nearly reached. In addition, the platinum damping bounces around the Ni reference, showing rather scattered behaviour, while this was in fact expected to plateau immediately, because the spin diffusion length is only 1-2nm. This is attributed to laser instability and an uncontrolled interface, both of which are discussed in the next chapter.

Upon inspecting the SSLW response, something else can be observed. The Ni damping time lies significantly above all the Pt samples and the Ni-Ti reference sample. This could mean that in this case the intrinsic damping within Ni is supplemented by some additional mechanism that is introduced with the Ti layer. One must, however, be careful with making conclusions here as the SAW data, as well as the sudden

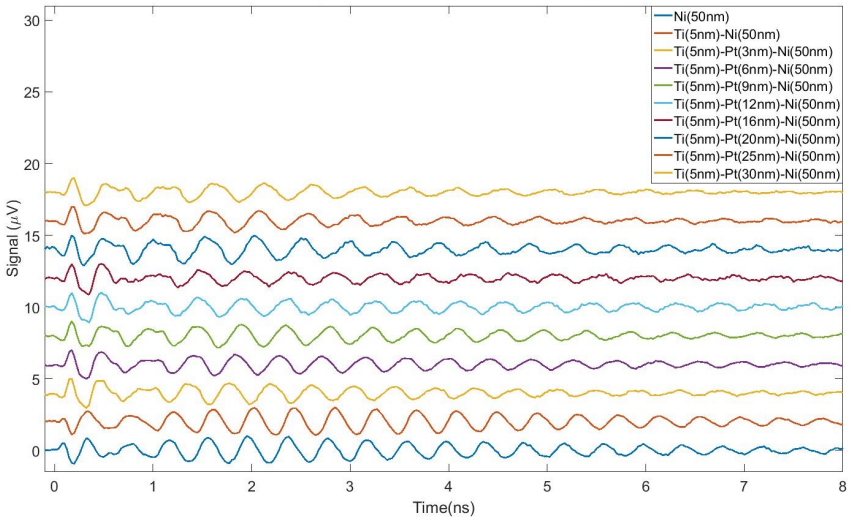

Figure 4.8: *Time traces of Pt samples at SAW resonance as a function of underlayer thickness.*

dip at $d_{Pt} = 16$ shows that uncertainty in these measurements may be larger than just that of the fits. However, since every single Pt data point lies significantly below that of the Ni, it is possible that spin wave pumping into the Ti layer occurs. If this is the case, the Ti layer already causes sufficient scattering to diffuse the spins, as the introduction of the Pt layer does not seem to shift the damping time further down by any significant amount. This may seem implausible since the layer thickness is only 5nm and the spin diffusion length is 13nm. However, due to the increase in temperature the phonon population rises and the spins have more opportunities to scatter, reducing the spin diffusion length [23]. This also means that the SSLW is far more efficient at pumping spins into the additional layers than the SAW. No evidence to either prove or discredit this was found in the literature.

For the Cu samples, the SSLW shows similar behaviour to the SAW for the larger thicknesses, but the thicknesses up to 12nm are very different. First of all, it is expected that the effect of the temperature redistribution is smaller than for the SAW, since the SAW is far more delocalized, but that in itself cannot explain why the damping times stay above the Ni-Ti reference for the SSLW, while for the SAW they are already far below it. Something, therefore, could be happening in the magnetization dynamics. A possible explanation is that introducing the layer of Cu between the Ni and Ti partially inhibits the spins from migrating into the Ti layer. Not only do they have to cross an additional interface, the relaxation time in Cu is far lower than in Ni or Ti and the Cu layer thickness is far below diffusion length, not nearly close enough for the temperature to make up. Since our detection scheme measures the precession in the entire sample, any spin precessing in Cu will also contribute to the signal. For the

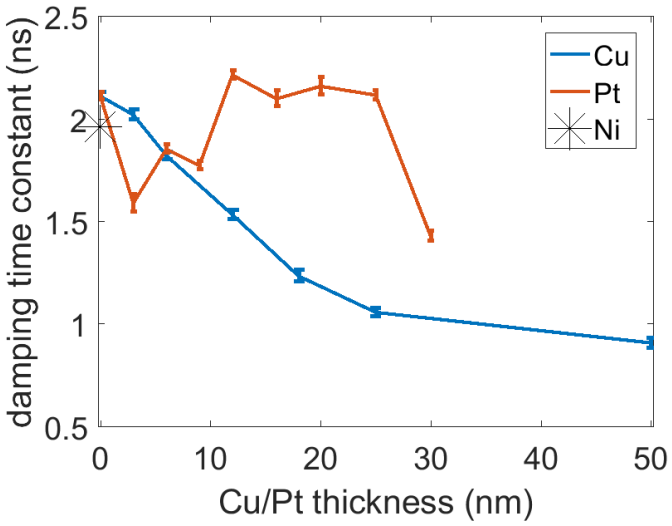

Figure 4.9: *Damping constants of the Faraday signal at SAW resonance as a function of underlayer thickness.*

larger Cu samples, this effect is overcome by the temperature sink effect that reduces the FMR and the damping time increases even beyond the point of that of Pt. This is supported by the fact that the same effect mitigating the damping is not observed for the Pt layer, since the 3nm sample already exceeds the spin diffusion length at room temperature, let alone the increased temperature the laser induces. However, the aberrant point at $d_{Pt} = 16$, begs the question whether the measurements were precise enough to warrant such a conclusion. However, the increased damping of the Pt and Ti-Ni samples, together with the mitigating effect that a small layer of Cu seems to have made this a very logical explanation of what has happened here.

The frequencies in the signal correspond well to the ones found in the field dependent scans and the acoustic signal. This is simply a result of the frequency shift of the driving force. Interestingly, however, it seems that for the CU sample a critical thickness of about 18nm must be reached before a significant change can be seen, while for the platinum every sample over 3nm already shows this behaviour. Furthermore, the frequencies of both the SAW and SSLW are more susceptible to the Pt layer than the Cu layer. Since the response of the acoustic modes depends on the ratio between the excitation wavelength, the thickness of the normal metal layer and the the Rayleigh wave velocities in the layer [48], one can only conclude that the wave velocities (both Rayleigh and longitudinal, and therefore also the shear) in Pt are smaller than in Cu. This is in accordance with theory and is a result mostly of its high density.

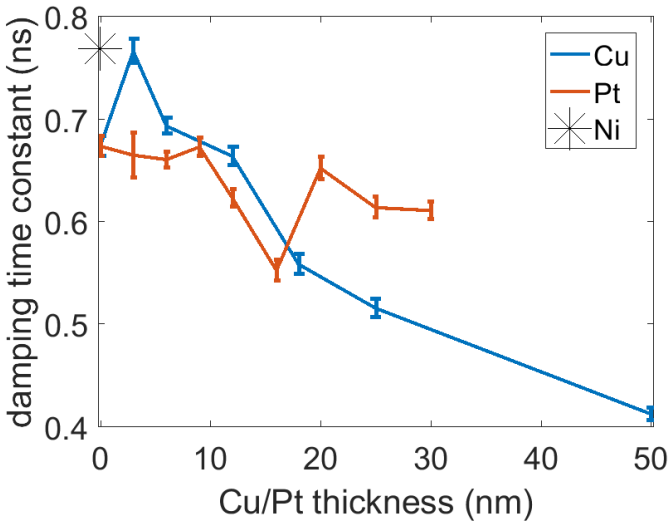

Figure 4.10: *Damping constants of the Faraday signal at SSLW resonance as a function of underlayer thickness.*

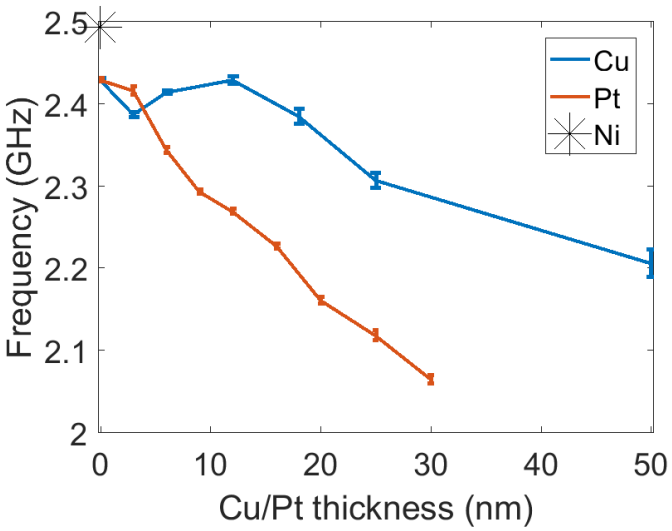

Figure 4.11: *Frequencies of the Faraday signal at SAW resonance.*

4.4 Anisotropy created by a PtO underlayer

For the platinum samples, the differences between a pure platinum layer and one with an oxide layer allowed to form on the Pt-Ni surface were investigated. This was done for 12nm and 25nm samples. The difference between the preparation of these samples and the ones described in chapter 3 is that the platinum layer in this case was exposed to air before growing the Ni layer on top of it. The results are shown in Figures 4.13 and 4.14, the first of which shows the time traces as a function of field, while the latter shows two time traces in particular, with different applied fields (in terms of direction). In these figures, it is obvious that the direction of the magnetic field changes the phase of the precession by 180 degrees. Moreover, a large background is present at small

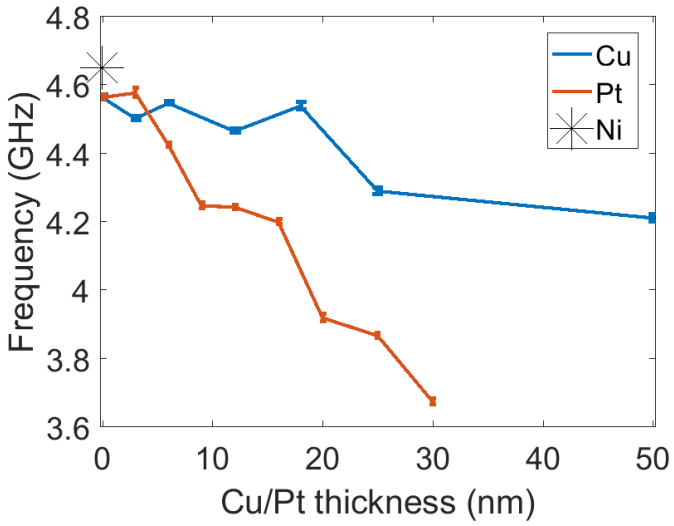

Figure 4.12: *Frequencies of the Faraday signal at SSLW resonance*

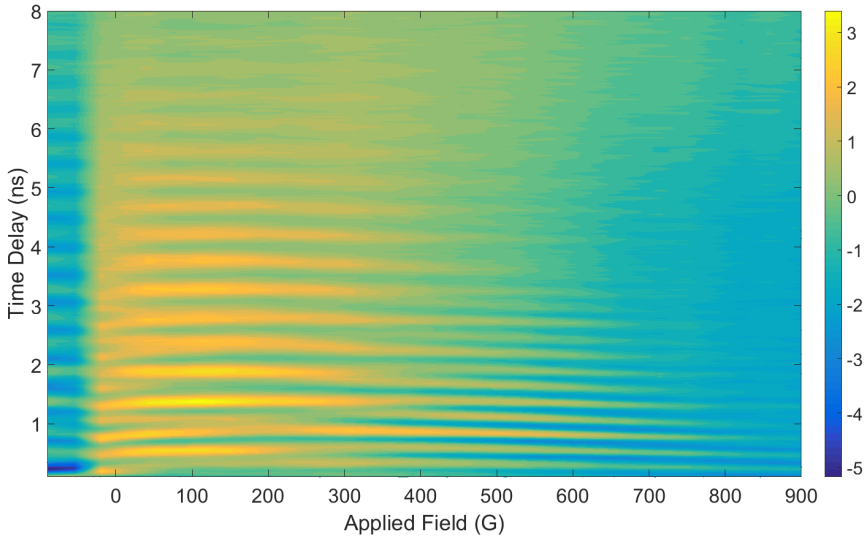

Figure 4.13: *Field dependent time traces of Pt sample with oxide layer.*

enough fields, which also flips sign along with the magnetic field. This background slowly decreases in strength when the applied field strength is increased. These results are indicative of magnetic anisotropy in the Ni film, since it is here where the precession of spins takes place. Apparently, the platinum oxide layer causes structure to form in the Ni film when it is grown. The most likely explanation for this is that the platinum oxide itself has structure, which the Ni film, which usually is completely isotropic, now follows. To investigate this anisotropy, an angle dependence measurement was performed, where the angle of magnetic field was varied (with respect to the horizon). The results are shown in Figure 4.15 and 4.16. Between 95 and 115 degrees, there is a large change in frequency of the signal as a result of only a small angle change. In addition a large dip where the signal falls off is observed in this region, after

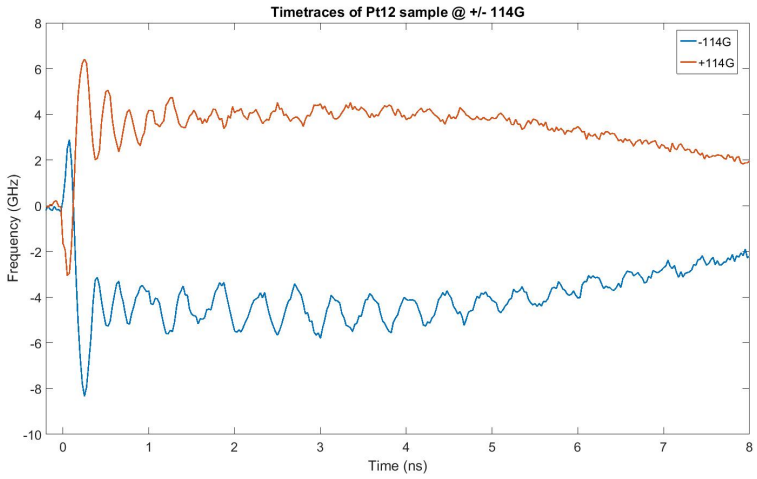

Figure 4.14: *Time traces at positive and negative field of the Pt sample with oxide layer, showing the phase shift with changing field sign.*

which the same phase shift is observed as was seen in Figure 4.14. Therefore, a hard magnetization axis must be present at this angle.

The reason the platinum oxide gains structure while the platinum does not is unknown. It seems, however, likely that this is the reason for the anisotropy in the Ni layer. It is an interesting thing to investigate, but it goes beyond the scope of this thesis to do so.

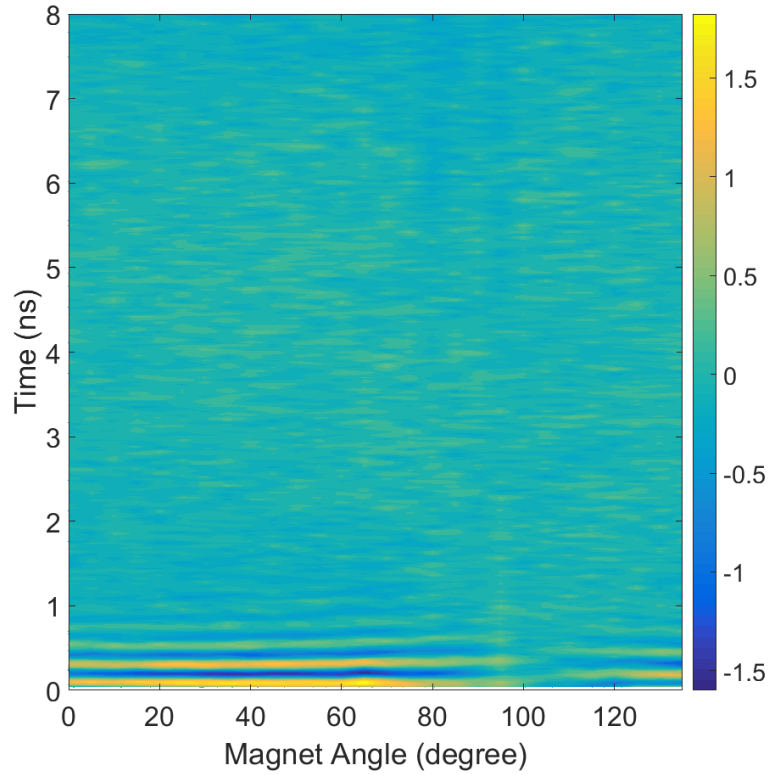

Figure 4.15: *Time trace of the angle dependence of Pt with oxide layer.*

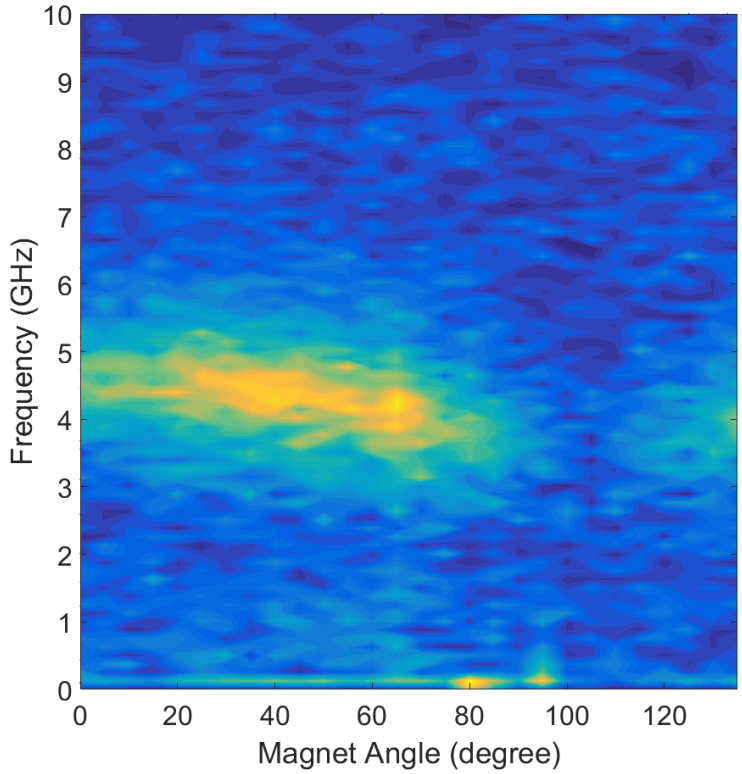

Figure 4.16: *Angle dependence of Pt with oxide layer, Fourier transformed.*

Chapter 5

Discussion

The acoustic signals fit well within the theory. The shift in frequency for all samples is as expected and even the increased damping exhibited by the Cu samples can be explained sufficiently by considering heat distribution. The magnetic response also fits the theory presented here, that is, within the framework of spin currents, spin wave pumping and spin diffusion. By considering scattering at the interfaces one can explain the rise in damping time for the thin Cu samples and the lack of a trend in the Pt samples is as expected. However, due to several issues that occurred with this experiment, the conclusions from the previous chapter, although carefully drawn, come with some side notes. In this chapter, the main problems with this experiment are treated.

First of all, although the thickness of the layers was known within a few Angstrom, no roughness measurements were done. This means that the interactions on the surface might vary for the different samples. Since interactions at the surface, such as magnon-electron interactions, play a role in the damping of the FMR [13], this could very well have affected the measurements.

Secondly, during the measurements, the laser that was used to both generate pump and probe pulses, experienced some severe issues, resulting in fluctuations in power. The instability of the system meant that fluence was no longer a dependable variable. As treated in section 3.5, the fluence strongly determines the observable signal due to thermal effects, and therefore becomes another source of uncertainty and might have caused the scattering of the data.

Thirdly, there are some influences that have to do with the nature of the experiment. Since the experiments were not done closely to any of the diffusion lengths (save for Ti but that thickness was not varied), it is hard to say meaningful things regarding spin wave pumping. The Cu could have shown increased damping for the larger samples due to some of the spin starting to diffuse, but this remains unknown due to the effect the thermal conductance had on both the acoustic driving and the correction factor

that the signal experiences due to a decrease in demagnetization, necessary to create contrast (see sections 2.1.3 and 3.5). The Pt did not show an increase in damping, which might be a consequence of the fact that the Ti already diffused the spins. The measurement does not distinguish in which layer the diffusion occurs and therefore this is equivalent.

Finally, there is the matter of intrinsic damping in the Ni films. The Ni film of 50nm has a nice, strong, signal, but is also subject to intrinsic mechanisms that might hinder the spin wave pumping. Since we are operating far above the spin diffusion length, a spin current that starts from the surface, will never reach the underlying layer. The only action can happen on a length scale of 10nm away from the FM/NM interface, but this is not where most of the laser energy is absorbed. It is therefore not certain if spin wave pumping plays a significant role. In addition, the intrinsic damping of the Ni might be so big that any additional mechanisms are small by comparison. Couple that with the laser instability and fluence dependence and one might have a hard time distinguishing whether or not something is happening. The result is that one can only speculate and resort to what was already known. However, the next chapter proposes fixes to some of these problems in order to avoid them in future experiments.

Chapter 6

Future experiments

In principle, the experiment presented here could hold valuable information on spin wave pumping in terms of efficiencies and spin diffusion lengths in different materials. In order to achieve relevant results however, the experiment has to be augmented.

First of all, the Ni thickness should be reduced as even with a experimental method that is sensitive to the entirety of the multilayer, little difference could be seen. In addition, thicknesses should be chosen close to the spin diffusion length in order to see the rise in damping upon approaching the value and the plateauing associated with higher thicknesses. Since the set-up depends on transmission this will only work for spin diffusion lengths below approximately 50-75nm, depending on the optical density of the material involved. Varying Ti, ironically, could be well suited. For this experiment it was only used as a way to ensure good adhesion of the other materials, but it can in and of itself be a very interesting material to investigate. Moreover, the material cannot have a large heat conductance, as any such materials might exhibit the same issues as Cu did in this experiment. One must always take care that the acoustics stay the same when comparing different samples to ensure that strong conclusions on the magnetization dynamics might be drawn. Alternatively, one could use a heat buffer layer. However, this would once again create an additional interface and one would have to take great care to operate below the spin diffusion length for said material. However, it does provide an additional benefit of shielding the material that is to be investigated from heating effects. Finally, more control on the interface between FM and NM would be beneficial for the experiment, as it would enable ruling out interfacial differences as a source of difference in for instance damping.

To conclude, two possible methods for examining damping and spin diffusion are presented, based on references [30], [29] and the findings of this experiment. The first method would consist of an experiment similar to the one presented here, but omitting the additional adhesion layer. To solve the issue of the thermal effect on the acoustics

and diffusion length in the material to be examined, a buffer layer is to be placed with small electron scattering probability and relatively low heat conductance. This will also ensure a strong acoustic signal in the Ni to remain. The Ni should be kept at 10nm thickness, despite the fact that this reduces the Faraday rotation amplitude, due to the decrease in path length through the relevant material. The other option would be to use a different material as a spin source. However, since ferromagnets have fundamentally short diffusion lengths, the latter might prove a challenge. If this path is followed, the spin diffusion length might be determined as the thickness for which the additional damping no longer increases with increasing thickness.

The second method would be to incorporate a known spin sink behind the sample, as shown in Figure 6.1. Several samples could then be constructed, varying the ma-

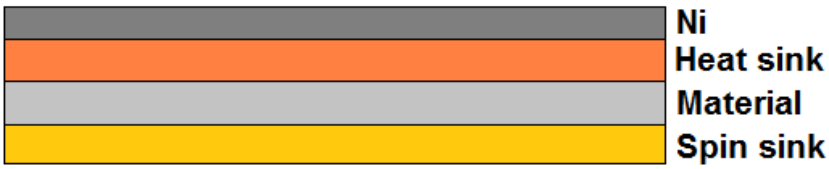

Figure 6.1: *Altered sample composition for a possible future experiment.*

terial of interest's thickness, for one set of samples containing the spin sink and one set without the spin sink. Both sets will converge to the same damping value as the thickness is increased, one from a place of higher damping (due to the spin sink) and one from a place of lower damping [29]. The value where they meet will be the spin diffusion length as it is there that the spin sink loses its effect, meaning that all the spins diffuse in the other material.

Chapter 7

Conclusion

An FMR experiment was performed on Ni-Cu-Ti and Ni-Pt-Ti multilayers using a TG set-up that directly maps strain fields in order to launch sounds waves with specific wavelength which drive magnetization dynamics in the Ni layer. Results were analyzed using field dependency scans and fitting parameters to examine behaviour under resonance conditions.

While the results of the frequency of both the acoustic signal and the Faraday signal followed the theory as expected, the damping of the magnetic response was somewhat less unambiguous. Nevertheless, all behaviour that was observed fits within the theoretical considerations regarding spin wave pumping. The lack of strong, irrefutable, conclusions lies in the uncertainty and the problems described in the discussion Several issues concerning the sample composition and laser stability collectively contributed to this.

Incorporating the Cu seemed to reduce the damping caused by the Ti at low thicknesses, but at higher thicknesses thermal redistribution caused additional damping in the signal, through the acoustics.

For the Pt samples, no additional damping was found with regard to the Ni-Ti reference. Finally, the addition of the Ti on the traditional Ni sample seemed to have already impacted damping in the case of SSLW resonance. This was, however, not found for the SAW, which has been shown to be able to drive spin wave pumping in other research, making this occurrence strange.

All of these effects were explained with theory. Nevertheless, though all have a fundamental basis in both theory and logic, they should not be taken as fact, due to all the problems discovered during the experiment. Instead, a method for improving the experiment for future uses was proposed that should severely increase performance.

Appendix A

Additional Theory

A.1 Exchange energy

Spins are not exclusively influenced by external magnetic fields. Since they themselves carry a magnetic moment, they also directly influence one another. This is called exchange interaction. The basic principles can be derived considering a two electron system. Upon writing down the wave function, there are two options. Either the system is in a symmetric singlet state (S=0) or in a anti-symmetric triplet state (S=1) [7]:

$$\Phi_S = \frac{1}{\sqrt{2}}[\phi_a(r_1)\phi_b(r_2) + \phi_a(r_2)\phi_b(r_1)]\chi_S \tag{A.1}$$

$$\Phi_T = \frac{1}{\sqrt{2}}[\phi_a(r_1)\phi_b(r_2) - \phi_a(r_2)\phi_b(r_1)]\chi_T \tag{A.2}$$

The energy difference between these two states can be written as follows:

$$E_S - E_T = 2\int \phi_a^*(r_1)\phi_b^*(r_2)\hat{H}\phi_a^*(r_2)\phi_b^*(r_1)dr_1dr_2 \tag{A.3}$$

For the singlet state $S_1 \cdot S_2 = -\frac{3}{4}$, whereas for the triplet state the dot product equals $\frac{1}{4}$. Hence, one arrives at an effective Hamiltonian:

$$\hat{H} = \frac{1}{4}(E_S + 3E_T) - (E_S - E_T)S_1 \cdot S_2 \tag{A.4}$$

The second term of this equation is spin dependent and describes an interaction between the two spins. Using this, one can define an exchange integral:

$$J = \int \phi_a^*(r_1)\phi_b^*(r_2)\hat{H}\phi_a^*(r_2)\phi_b^*(r_1)dr_1dr_2 \tag{A.5}$$

If one considers that in many electron systems interactions such as these might occur between all electrons on neighbouring atoms, one arrives at the Hamiltonian of the Heisenberg model:

$$\hat{H} = -\sum_{ij} J_{ij} S_i \cdot S_j \tag{A.6}$$

Usually, the assumption is made that the interaction between spins is independent of i and j and only nearest neighbours are taken into the sum, which is a reasonable approximation in many cases.

In ferromagnets, the exchange interactions lead to an exchange field, given by:

$$B_m = \lambda M, \tag{A.7}$$

where λ is a constant and M the total magnetization. Whether or not a material will exhibit ferromagnetic behaviour depends on the strength of this field. For a quantitative analysis of this, consider flipping part of the equilibrium spins. This corresponds in Figure 2.1 to moving the electrons nearest the Fermi energy into the other band up to an energy $E_F + \delta E$. In this configuration each single electron is moved δE up in energy and the amount of electrons that experiences this shift is equal to the density of states at the Fermi energy (in first approximation) multiplied by δE. Therefore, the energy cost is given by:

$$\Delta E_K = -\frac{1}{2} g(E_F)(\delta E)^2 \tag{A.8}$$

However, the molecular field will constitute a counter effect equal to:

$$\Delta E_M = -\int_0^M \mu_0 \lambda M^* dM^* = -\frac{1}{2}\mu_0 \lambda M^2, \tag{A.9}$$

where M is given by the difference in spins up and down, multiplied by their individual magnetic moment, the Bohr Magneton (μ_B). Defining $U = \mu_0 \mu_B^2 \lambda$, the total increase energy of the combined effects is given by:

$$\Delta E = \frac{1}{2} g(E_F)(\delta E)^2 (1 - U g(E_F)) \tag{A.10}$$

The Stoner criterion is then:

$$U g(E_F) \geqslant 1, \tag{A.11}$$

since fulfilling this constitutes a decrease in overall energy by spontaneous magnetization.

λ is independent of temperature. However, the saturation magnetization that arises from the exchange field is not and in fact disappears above a certain temperature,

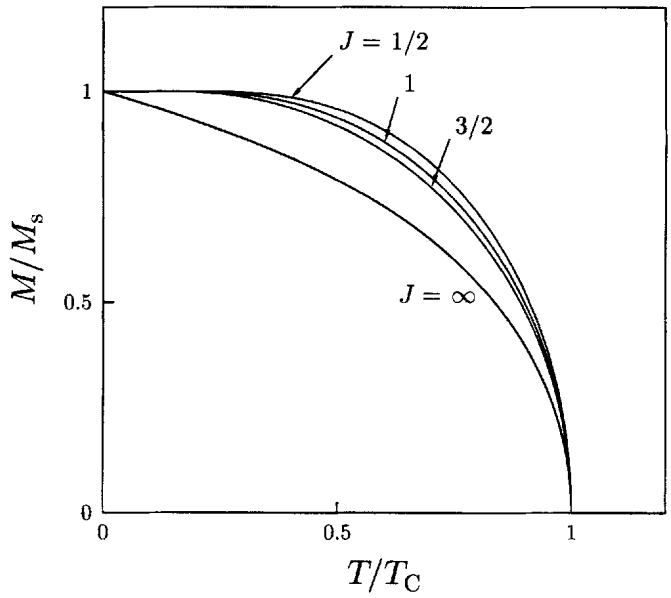

Figure A.1: *Normalized mean field strength as a function of the temperature relative to T_C. Adapted from [7].*

called the Curie Temperature (T_C). For its derivation the reader is directed to [7]. For illustrative purposes the solution is shown in Figure A.1 for different values of the total angular momentum, J (Note that this J=L+S and is different from the exchange integral). The discontinuity in the gradient of the magnetization at $T = T_C$ signifies a

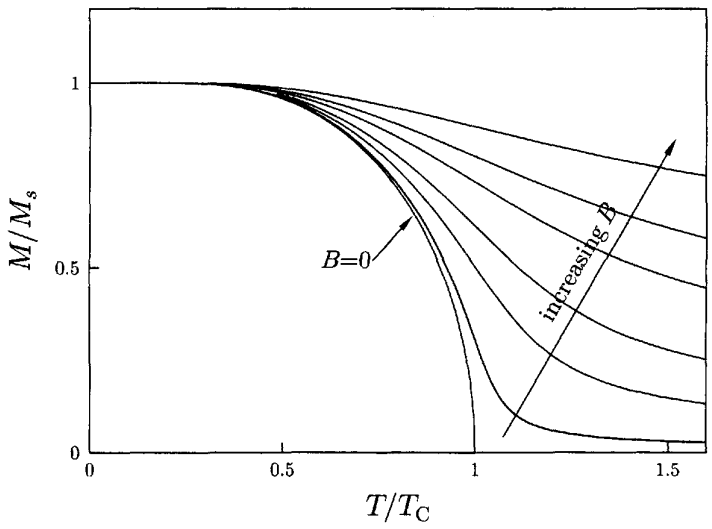

Figure A.2: *Normalized mean field strength as a function of the temperature relative to T_C for different applied fields (B). Adapted from [7].*

(second order) phase transition from the ferromagnetic state to an ordinary paramagnetic state for higher temperatures. Interestingly, upon applying a magnetic field, this

phase transition disappears, as can be seen in Figure A.2, since now there is always an energetic reason for magnetization moments to line up.

A.2 Quantum mechanical derivation of LLG equation

To derive the LLG equation quantum mechanically, one starts from the commutator with the Hamiltonian operator [49]:

$$i\hbar\frac{dS}{dt} = [S, \hat{H}] \tag{A.12}$$

The Hamiltonian follows once again from the energetic interaction of the spin with the surrounding magnetic field, in accordance with equation 2.2. Using both equations and writing H_{eff} for the effective magnetic field, one can derive the z component of the commutator:

$$\begin{aligned}[S_Z, H] &= -\frac{g\mu_B}{\hbar}[S_z, S \cdot H_{eff}] \\ &= -\frac{g\mu_B}{\hbar}([S_z, S_x]H_{effx} + [S_Z, S_y]H_{effy})\end{aligned}$$

Making use of the commutation rule $[S_i, S_j] = i\hbar\epsilon_{ijk}S_k$:

$$\begin{aligned}[S_Z, H] &= ig\mu_B(H_{effy}S_x + H_{effx}S_y) \\ &= ig\mu_B(S \times H_{eff})_x\end{aligned}$$

Combinig these with the results for the other two cartesian coordinates leads to the equation of motions for spins:

$$\frac{dS}{dt} = \frac{g\mu_B}{\hbar}(S \times H_{eff}) \tag{A.13}$$

Since the accumulation of spin results in an internal magnetization, this can be rewritten in terms of total magnetization:

$$\frac{dM}{dt} = -\gamma\mu_0 M \times H_{eff} \tag{A.14}$$

A.3 FMR in the LLG equation and modes other than the Kittel mode

The driving force on the precession resulting from the sound waves is incorporated into the traditional LLG equation through modification of the effective field [14, 15]. Since the effective field is given by:

$$H_{eff} = -\nabla_m F, \tag{A.15}$$

where F is the magnetic free energy, one can incorporate the FMR by looking at its effect thereon. In the absence of acoustics and anisotropy, the magnetic free energy is given by:

$$F_0 = -\mu_0 H \cdot \frac{M}{M_S} + C_1 \tag{A.16}$$

Here C_1 is a constant and M_S is the saturation magnetization. Since a sound wave is nothing more than a spatially modulated strain, it contributes to the magnetic free energy through this strain and a term is added. Assuming a sound wave propagating in the x direction:

$$F = F_0 + F_{FMR} = -\mu_0 H \cdot \frac{M}{M_S} + B_1 \epsilon(x,t)(\frac{M_x}{M_S})^2 + C, \tag{A.17}$$

where B_1 is the magneto-elastic coupling constant and ϵ is the strain field. So called back-action of the magnetization on the acoustic signal is also possible [14]. Dreher et al. show a detailed discussion of how the magnetization influences the elastic free energy, analogous to the discussion of the inverse effect above.

Apart from the coherent Kittel mode, two other spin waves can be identified, namely standing spin waves (SSW) and the Damon-Eschbach mode [30, 50]. Walowski et al. reported all of these modes in Ni films, depending on thickness as shown in Figure A.3. Standing spin waves are a result of the role of exchange interactions and the finite thickness of the film that causes confinement of the spin waves as depicted in Figure A.4 [9]. As can be seen in Figure A.3, these spin waves can only exist in thin layers. For thick layers, the Damon Eschbach mode, which relies on longer ranges where magnetic dipolar interactions start to take over. Both modes are shifted in frequency from the Kittel mode. Detailed formulae of these can be found in reference [30]

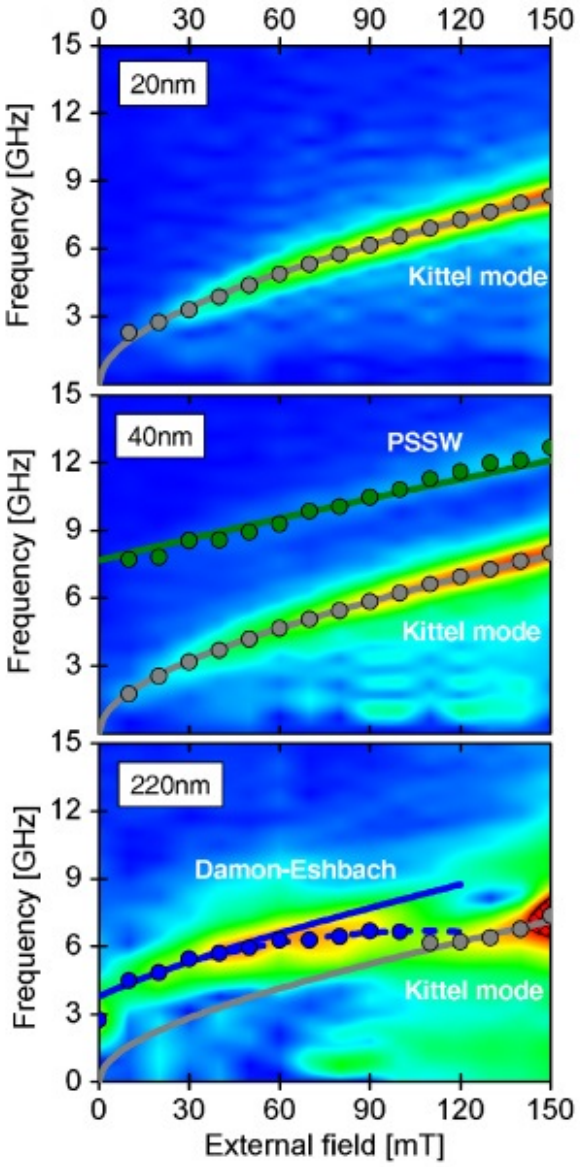

Figure A.3: *Fourier power spectra as color maps for three Ni thicknesses tNi = 20, 40 and 220nm. Figure and caption adapted from [30].*

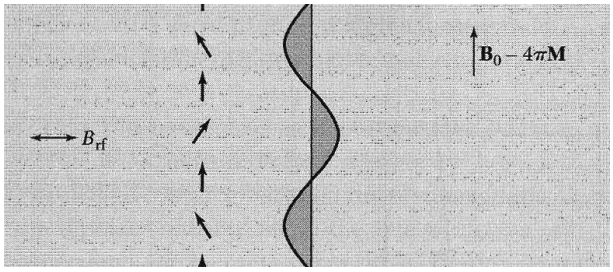

Figure A.4: *Standing Spin Wave in a thin film, excited as a result of a static magnetic field perpendicular to the film in addition to a radio frequency magnetic field parallel. Adapted from [9].*

A.4 Derivation of the Kittel equation

Kittel considered the equation of motion given by the Landau-Lifshitz equation (eq. 2.12) and assumed a static applied field B along the z axis. This means that the only components of M will lie orthogonal to this direction and are given by:

$$\frac{dM_z}{dt} = \gamma(M_y B_z^i - M_z B_y^i) = \gamma[B_0 + (N_y - N_z)M]M_x \tag{A.18}$$

$$\frac{dM_y}{dt} = \gamma[M(-N_x M_x) - M_x(B_0 - N_z M)] = -\gamma[B_0 + (N_x - N_z)M]M_x \tag{A.19}$$

where N_j are the demagnetization factors and a ellipsoidal sample is assumed. $\frac{dM_z}{dt}$ is approximated to be zero and M_z is considered equal to M. A solution to these two equations exists if the determinant vanishes, i.e.:

$$\begin{vmatrix} i\omega & \gamma[B_0 + (N_y - N_z)M] \\ -\gamma[B_0 + (N_x - N_z)M] & i\omega \end{vmatrix} = 0, \tag{A.20}$$

The result is the Kittel equation:

$$\omega^2 = \gamma^2[B_0 + (N_y - N_z)M][B_0 + (N_x - N_z)M], \tag{A.21}$$

A.5 The Spin Seebeck effect & spin currents

The Spin Seebeck effect occurs when a temperature gradient is present in a magnet [51]. Similar to the ordinary Seebeck effect, which generates an ordinary voltage, the Spin Seebeck effect generates a spin voltage, that can drive a spin current. Here, it is the magnons that carry the spin information, as opposed to the conduction electrons, as evidenced by the long length scales over which this effect persists [52].

The Spin current resulting from either Spin Seebeck effect or spin wave pumping depends on the voltage difference $n_{\uparrow,\downarrow}$ and the diffusion dynamics of the spins:

$$\frac{n_{\uparrow,\downarrow}}{\tau_S} = D_e \frac{\delta^2 n_{\uparrow,\downarrow}}{\delta x^2} \tag{A.22}$$

The spin difference as a result of the current is determined by the density of states at the Fermi energy $D(E_F)$ and the spin voltage V_S:

$$n_\uparrow - n_\downarrow = D(E_F)[\mu_\uparrow - \mu_\downarrow] = D(E_F)eV_S \tag{A.23}$$

Here, μ is the chemical potential of the spin up and down bands. Solving this equation

for the voltage leads to:

$$\Delta\mu = \Delta\mu_0 e^{\frac{-x}{l_S}}, \tag{A.24}$$

which is similar to what was seen in Figure 2.7. This opens up the spin diffusion length to direct measurement.

Bibliography

[1] E. Belin-Ferre, *Mechanical properties of complex intermetallics*, World Scientific Publishing, 2011.

[2] M. V. Costache, S. M. Watts, C. H. van der Wal, and B. J. van Wees, *Electrical detection of spin pumping: dc voltage generated by ferromagnetic resonance at ferromagnet/nonmagnet contact*, Phys. Rev. B **78**, 064423 (2008).

[3] H. An, Y. Kanno, T. Tashiro, Y. Nakamura, J. Shi, and K. Ando, *Spin current transport in ceramic: TiN thin film*, Applied Physics Letters **108**, 121602 (2016).

[4] K. ichi Uchida, T. An, Y. Kajiwara, M. Toda, and E. Saitoh, *Surface-acoustic-wave-driven spin pumping in Y3Fe5O12/Pt hybrid structure*, Applied Physics Letters **99**, 212501 (2011).

[5] V. Castel, N. Vlietstra, J. B. Youssef, and B. J. van Wees, *Platinum thickness dependence of the inverse spin-Hall voltage from spin pumping in a hybrid yttrium iron garnet/platinum system*, Applied Physics Letters **101**, 132414 (2012).

[6] J. Coey, *Magnetism and Magnetic Materials*, Cambridge University press, 2009.

[7] S. Blundell, *Magnetism in condensed matter*, Oxford university press, 2001.

[8] J. Miltat, G. Albuquerque, and A. Thiaville., *Spin Dynamics in Confined Magnetic Structures I*, Springer-Verlag Berlin Heidelberg, 2001.

[9] C. Kittel, *An introduction to solid state physics*, John Wiley & Sons, inc., 2005.

[10] F. J. Dyson, *General Theory of Spin-Wave Interactions*, Phys. Rev. **102**, 1217 (1956).

[11] H. Adachi and S. Maekawa, *Theory of the acoustic spin pumping*, Solid State Communications **198**, 22 (2014), SI: Spin Mechanics.

[12] H. Keshtgar, M. Zareyan, and G. E. Bauer, *Acoustic parametric pumping of spin waves*, Solid State Communications **198**, 30 (2014).

[13] Y. Tserkovnyak, A. Brataas, and G. E. W. Bauer, *Enhanced Gilbert Damping in Thin Ferromagnetic Films*, Phys. Rev. Lett. **88**, 117601 (2002).

[14] L. Dreher, M. Weiler, M. Pernpeintner, H. Huebl, R. Gross, M. S. Brandt, and S. T. B. Goennenwein, *Surface acoustic wave driven ferromagnetic resonance in nickel thin films: Theory and experiment*, Phys. Rev. B **86**, 134415 (2012).

[15] M. Weiler, L. Dreher, C. Heeg, H. Huebl, R. Gross, M. S. Brandt, and S. T. B. Goennenwein, *Elastically Driven Ferromagnetic Resonance in Nickel Thin Films*, Phys. Rev. Lett. **106**, 117601 (2011).

[16] M. C. Hickey and J. S. Moodera, *Origin of Intrinsic Gilbert Damping*, Phys. Rev. Lett. **102**, 137601 (2009).

[17] E. Barati, M. Cinal, D. M. Edwards, and A. Umerski, *Gilbert damping in magnetic layered systems*, Phys. Rev. B **90**, 014420 (2014).

[18] T. Kasuya and R. C. LeCraw, *Relaxation Mechanisms in Ferromagnetic Resonance*, Phys. Rev. Lett. **6**, 223 (1961).

[19] C. Kittel, *Ferromagnetic resonance*, J. Phys. Radium **12**, 291 (1951).

[20] M. Farle, *Ferromagnetic resonance of ultrathin metallic layers*, Reports on Progress in Physics **61**, 755 (1998).

[21] L. Eudenilson, G. Albuquerque, and M. Cottam, *Polaritons in Periodic and Quasiperiodic Structures*, Elsevier, 2004.

[22] D. Fang, H. Kurebayashi, J. Wunderlich, K. Výborný, L. Zârbo, R. Campion, A. Casiraghi, B. Gallagher, T. Jungwirth, and A. Ferguson, *Spin-orbit-driven ferromagnetic resonance*, Nature Nanotechnology **6**, 413 (2011).

[23] M. Isasa, E. Villamor, L. E. Hueso, M. Gradhand, and F. Casanova, *Temperature dependence of spin diffusion length and spin Hall angle in Au and Pt*, Phys. Rev. B **91**, 024402 (2015).

[24] M.-H. Nguyen, D. C. Ralph, and R. A. Buhrman, *Spin Torque Study of the Spin Hall Conductivity and Spin Diffusion Length in Platinum Thin Films with Varying Resistivity*, Phys. Rev. Lett. **116**, 126601 (2016).

[25] T. Kimura, T. Sato, and Y. Otani, *Temperature Evolution of Spin Relaxation in a* NiFe/Cu *Lateral Spin Valve*, Phys. Rev. Lett. **100**, 066602 (2008).

[26] M. Weiler, H. Huebl, F. S. Goerg, F. D. Czeschka, R. Gross, and S. T. B. Goennenwein, *Spin Pumping with Coherent Elastic Waves*, Phys. Rev. Lett. **108**, 176601 (2012).

[27] B. L. Zink, M. Manno, L. O'Brien, J. Lotze, M. Weiler, D. Bassett, S. J. Mason, S. T. B. Goennenwein, M. Johnson, and C. Leighton, *Efficient spin transport through native oxides of nickel and permalloy with platinum and gold overlayers*, Phys. Rev. B **93**, 184401 (2016).

[28] P. A. Deymier, J. O. Vasseur, K. Runge, A. Manchon, and O. Bou-Matar, *Phonon-magnon resonant processes with relevance to acoustic spin pumping*, Phys. Rev. B **90**, 224421 (2014).

[29] S. Yakata, Y. Ando, T. Miyazaki, and S. Mizukami, *Temperature Dependences of Spin-Diffusion Lengths of Cu and Ru layers*, Japanese Journal of Applied Physics **45**, 3892 (2006).

[30] J. Walowski, M. D. Kaufmann, B. Lenk, C. Hamann, J. McCord, and M. Münzenberg, *Intrinsic and non-local Gilbert damping in polycrystalline nickel studied by Ti:sapphire laser fs spectroscopy*, Journal of Physics D: Applied Physics **41**, 164016 (2008).

[31] E. Hecht, *Optics*, Addison Wesley, 2002.

[32] J. Janušonis, C. L. Chang, T. Jansma, A. Gatilova, V. S. Vlasov, A. M. Lomonosov, V. V. Temnov, and R. I. Tobey, *Ultrafast magnetoelastic probing of surface acoustic transients*, Phys. Rev. B **94**, 024415 (2016).

[33] A. Weiner, *Ultrafast Optics*, John Wiley & Sons, inc., 2009.

[34] J. Roger, A. Maznev, M. Banet, and K. Nelson, *Optical generation and characterization of acoustic Waves in thin films: fundamentals and applications*, Annu. Rev. Mater. Sci. **30**, 117 (2000).

[35] J. Janušonis, T. Jansma, C. L. Chang, and R. I. Tobey, *Transient Grating Spectroscopy in Magnetic Thin Films: Simultaneous Detection of Elastic and Magnetic Dynamics*, Scientific reports **6**, 29143 (2016).

[36] A. R. Duggal, J. A. Rogers, and K. A. Nelson, *Realtime optical characterization of surface acoustic modes of polyimide thinfilm coatings*, Journal of Applied Physics **72**, 2823 (1992).

[37] J. Rogers, Y. Yang, and K. Nelson, *Elastic modulus and in-plane thermal diffusivity measurements in thin polyimide films using symmetry-selective real-time impulsive stimulated thermal scattering*, Applied Physics A **58**, 523 (1994).

[38] H. Carslaw and J. Jaeger, *Conduction of heat in solids*, Oxford university press, 1959.

[39] J. A. Rogers, A. A. Maznev, M. J. Banet, and K. A. Nelson, *Optical Generation and Characterization of Acoustic Waves in Thin Films: Fundamentals and Applications*, Annual Review of Materials Science **30**, 117 (2000).

[40] R. M. Slayton, K. A. Nelson, and A. A. Maznev, *Transient grating measurements of film thickness in multilayer metal films*, Journal of Applied Physics **90**, 4392 (2001).

[41] J. A. Rogers and K. A. Nelson, *Photoacoustic determination of the residual stress and transverse isotropic elastic moduli in thin films of the polyimide PMDA/ODA*, IEEE Transactions on Ultrasonics, Ferroelectrics, and Frequency Control **42**, 555 (1995).

[42] M. Weiler, L. Dreher, C. Heeg, H. Huebl, R. Gross, M. S. Brandt, and S. T. B. Goennenwein, *Elastically Driven Ferromagnetic Resonance in Nickel Thin Films*, Phys. Rev. Lett. **106**, 117601 (2011).

[43] C. E. Moreau, I. C. Moraru, N. O. Birge, and W. P. P. Jr., *Measurement of spin diffusion length in sputtered Ni films using a special exchange-biased spin valve geometry*, Applied Physics Letters **90**, 012101 (2007).

[44] E. Beaurepaire, J.-C. Merle, A. Daunois, and J.-Y. Bigot, *Ultrafast Spin Dynamics in Ferromagnetic Nickel*, Phys. Rev. Lett. **76**, 4250 (1996).

[45] C. Pool, *Encyclopedic dictionary of condensed matter physics*, Elsevier, 2004.

[46] L. Kinsler, A. Frey, A. Coppens, and J. Sanders, *Fundamentals of acoustics*, Wiley & sons, 2000.

[47] R. M. White, *Surface Elastic Waves*, Proceedings of the IEEE **58** (1970).

[48] A. R. Duggal, J. A. Rogers, and K. A. Nelson, *Realtime optical characterization of surface acoustic modes of polyimide thinfilm coatings*, Journal of Applied Physics **72**, 2823 (1992).

[49] M. Kaufmann, *Magnetization dynamics in all-optical pump-probe experiments: spin-wave modes and spin-current damping*, PHD-thesis, Götingen (2006).

[50] J. R. Eshbach and R. W. Damon, *Surface Magnetostatic Modes and Surface Spin Waves*, Phys. Rev. **118**, 1208 (1960).

[51] K. Uchida, H. Adachi, T. An, T. Ota, M. Toda, B. Hillebrands, S. Maekawa, and E. Saitoh, *Long-range spin Seebeck effect and acoustic spin pumping*, Nature materials **10**, 737 (2011).

[52] H. Adachi, K. ichi Uchida, E. Saitoh, and S. Maekawa, *Theory of the spin Seebeck effect*, Reports on Progress in Physics **76**, 036501 (2013).